Visual Dexterity: In-hand Dexterous Manipulation from Depth

Tao Chen^{1,2}, Megha Tippur², Siyang Wu³, Vikash Kumar⁴, Edward Adelson², Pulkit Agrawal*^{1,2}

¹Improbable AI Laboratory, Cambridge, MA 02139, USA
²Department of Electrical Engineering and Computer Science, Massachusetts Institute of Technology,
Cambridge, MA 02139, USA

³Institute for Interdisciplinary Information Sciences, Tsinghua University, Beijing, 100084, China ⁴Meta AI, Pittsburgh, PA 15213, USA

*To whom correspondence should be addressed; E-mail: pulkitag@mit.edu.

In-hand object reorientation is necessary for performing many dexterous manipulation tasks, such as tool use in unstructured environments that remain beyond the reach of current robots. Prior works built reorientation systems that assume one or many of the following specific circumstances: reorienting only specific objects with simple shapes, limited range of reorientation, slow or quasistatic manipulation, the need for specialized and costly sensor suites, simulation-only results, and other constraints which make the system infeasible for real-world deployment. We overcome these limitations and present a general object reorientation controller that is trained using reinforcement learning in simulation and evaluated in the real world. Our system uses readings from a single commodity depth camera to dynamically reorient complex objects by any amount in real time. The controller generalizes to novel objects not used during training. It is successful in the most challenging test: the abil-

ity to reorient objects in the air held by a downward-facing hand that must counteract gravity during reorientation. The results demonstrate that the policy transfer from simulation to the real world can be accomplished even for dynamic and contact-rich tasks. Lastly, our hardware only uses open-source components that cost less than five thousand dollars. Such construction makes it possible to replicate the work and democratize future research in dexterous manipulation. Videos are available at: https://taochenshh.github.io/projects/visual-dexterity.

Summary

A real-time controller that dynamically reorients complex and novel objects by any amount using a single depth camera.

Introduction

The dexterity of the human hand is vital to a wide range of daily tasks such as re-arranging objects, loading dishes in a dishwasher, fastening bolts, cutting vegetables, and other forms of tool use both inside and outside households. Despite a long-standing interest in creating similarly capable robotic systems, current robots are far behind in their versatility, dexterity, and robustness. In-hand object reorientation, illustrated in Figure 1, is a specific dexterous manipulation problem where the goal is to manipulate a hand-held object from an arbitrary initial orientation to an arbitrary target orientation (I–T). Object reorientation occupies a special place in manipulation because it is a pre-cursor to flexible tool use. After picking a tool, the robot must orient the tool in an appropriate configuration to use it. For example, a screwdriver can only be used if it is oriented in a manner that aligns the head with the top of the screw. Object reorientation is, therefore, not only a litmus test for dexterity but also an enabler for

many downstream manipulation tasks.

A reorientation system ready for the real world should satisfy multiple criteria: it should be able to reorient objects into any orientation, generalize to new objects, and operate in real-time using data from commodity sensors. Some seemingly benign setup choices can make the system impractical for real-world deployment. For instance, consider the choice of placing multiple cameras around the workspace to reduce occlusion in viewing the object being manipulated (8,9). For a mobile manipulator, such camera placements are impractical. Similarly, performing reorientation under the assumption that the hand is below the object (i.e., upwards facing hand configuration) (8-10) instead of the hand holding the object from the top (i.e., downwards facing hand configuration) is much easier. With a downward-facing hand, the hand must manipulate the object while simultaneously counteracting gravity. Small errors in finger motion can result in the object falling down. The upward-facing hand assumption makes control easier, but it limits the downstream use of the reorientation skill in many tool-use applications.

Even without real-world setup constraints, object reorientation is challenging because it requires coordinated movement between multiple fingers resulting in a high-dimensional control space. The robot must control the amount of applied force, when to apply it, and where the fingers should make and break contact with the object. The combination of continuous and discrete decisions leads to a challenging optimization problem that is often cast into mixed-integer programming, which is known to be NP-hard (11). To make computation feasible, a majority of prior works constrain manipulation to simple convex shapes such as polygons or cylinders (6, 8, 12–23). Other simplifying assumptions include designing specific movement patterns of fingers (19, 24), assuming fingers never make break contact with the object (16, 25), hand being in upwards facing configuration (5, 8, 10) or the manipulation being quasi-static (24, 26). Such assumptions restrict the applicability of reorientation to a limited set of objects, scenarios, or orientations (e.g., along only a single axis).

Complementary to the problem of control is measuring the state information required by the controller, such as the pose of the object, surface friction, whether the finger is in contact with the object or not, etc. Touch sensors provide local contact information but are not widely available as a plug-and-play module. The difficulty in using visual sensing is that the object is occluded by fingers during reorientation. Recent works employed RGBD cameras to estimate object pose but require a separate pose estimator to be trained per object, which limits their generalization to novel objects (8, 9, 24, 27).

Due to challenges both in perception and control, no prior work has demonstrated a real-world ready reorientation system. While controlling directly from perception is hard, given the oracle's low-dimensional representation of relevant state information such as the object's position, velocity, pose, and manipulator's proprioceptive state, it is possible to build a controller using deep reinforcement learning (RL) that successfully reorients diverse objects in simulation (7). RL effectively leverages large amounts of interaction data to bypass the continuous-discrete optimization problem. However, as a result of requiring large amounts of data and oracle state information, today, such RL controllers can only be trained in simulation. This leaves two open questions: how to train controllers with visual inputs and whether controllers trained in simulation will transfer to the real world (i.e., sim-to-real transfer problem).

The difficulty in training RL controllers from visual inputs stems from the learner's need to simultaneously solve the problem of inferring the relevant state information (i.e., feature learning) and determining the optimal actions. If the optimal actions were known in advance, it would be simpler to train a model that predicts these actions from visual inputs (i.e., supervised learning). Such a two-stage *teacher-student* training paradigm, where first a control policy is trained via RL with oracle state information (i.e., teacher) and then a second *student* policy trained via supervised learning to mimic the *teacher* has been successfully used for some applications (7, 28–31). We found the major roadblock in learning a visual policy that works across

diverse objects is the slow speed of rendering which resulted in training times of over 20 days with our compute resources. Such slow training makes experimentation infeasible. We devised a two-stage approach for training the vision policy that first uses a synthetic point cloud without the need for rendering and is then finetuned with rendered point cloud to minimize the sim-to-real gap. Our pipeline makes training $5\times$ times faster. The second consideration was the use of a sparse convolution neural network to represent the policy to process point clouds at speed required for real-time feedback control (12Hz in our case). By directly predicting actions from point clouds, our approach bypasses the problem of consistently defining pose/keypoints across different objects, allowing for generalization to new shapes.

The next challenge is in overcoming the sim-to-real gap. In recent years, locomotion controllers trained in simulation with RL have enabled quadrupeds to traverse diverse and natural terrains in the real world (30–32). In locomotion, the robot moves, but the ground remains stationary. During in-hand object reorientation, both the robot and the object move. Furthermore, a quadruped can almost always switch to a statically stable configuration, unlike reorientation with a downward facing hand where control failures are irreversible. Therefore, object reorientation requires more precise control and poses a harder sim-to-real transfer challenge. Some reasons for *sim-to-real* gap are differences in motor/object dynamics, perception noise, and modeling approximations made by the simulator. For instance, it is well-known that contact models in the simulation are a crude approximation of reality, especially for non-convex objects. Whether sim-to-real transfer of reorientation controller is even possible for such objects remained unclear.

The systematic choices of identifying simulated robot's dynamics parameters using real-world data (i.e., system identification or *real-to-sim*), domain randomization (33), design of reward function and the hardware considerations including the number of fingers and the fingertip material enabled us to overcome the sim-to-real gap. We conducted experiments in the

challenging downward-facing hand configuration and tested the controller's ability to make use of an external support surface for reorientation (i.e., extrinsic dexterity (34)) and the harder condition when the object is in the air without any supporting surface. The results demonstrate success in designing real-time controller that can dynamically reorient novel objects with complex shapes and diverse materials by any amount in the full space of rotations (SO(3)) using inputs from just a single commodity depth camera and joint encoders. While our system has imperfections, to the best of our knowledge, we present the first demonstration of real-world object reorientation in its full generality. Our results provide convincing evidence that sim-to-real transfer is possible for challenging dynamic and contact-rich manipulation tasks.

Finally, many prior efforts have used custom or expensive manipulators (such as the Shadow Hand (8-10) costing over \$100K) and often relied on sophisticated sensing equipment such as a motion capture system. Such a hardware stack is hard to replicate due to its cost and complexity. In contrast, our entire hardware setup costs less than \$5K and uses only open-source components making it easier to replicate. Furthermore, our platform is not specific to object reorientation and can be used for other dexterous manipulation tasks. Due to the low barrier to entry, and the evidence that a low-cost system can solve a challenging manipulation problem, our research platform can democratize research in dexterous manipulation.

Results

We trained a single controller to reorient 150 objects from an arbitrary initial to a target configuration in simulation. The learned controllers are deployed in the real world on the open-source three-fingered D'Claw manipulator (35) and a modified four-fingered version with nine and twelve degrees of freedom (DoFs), respectively. The robot's observation is a depth image captured from a single Intel RealSense camera and the proprioceptive state of the fingers. The goal is provided as the point cloud of the object in a target configuration in the SO(3) space. The

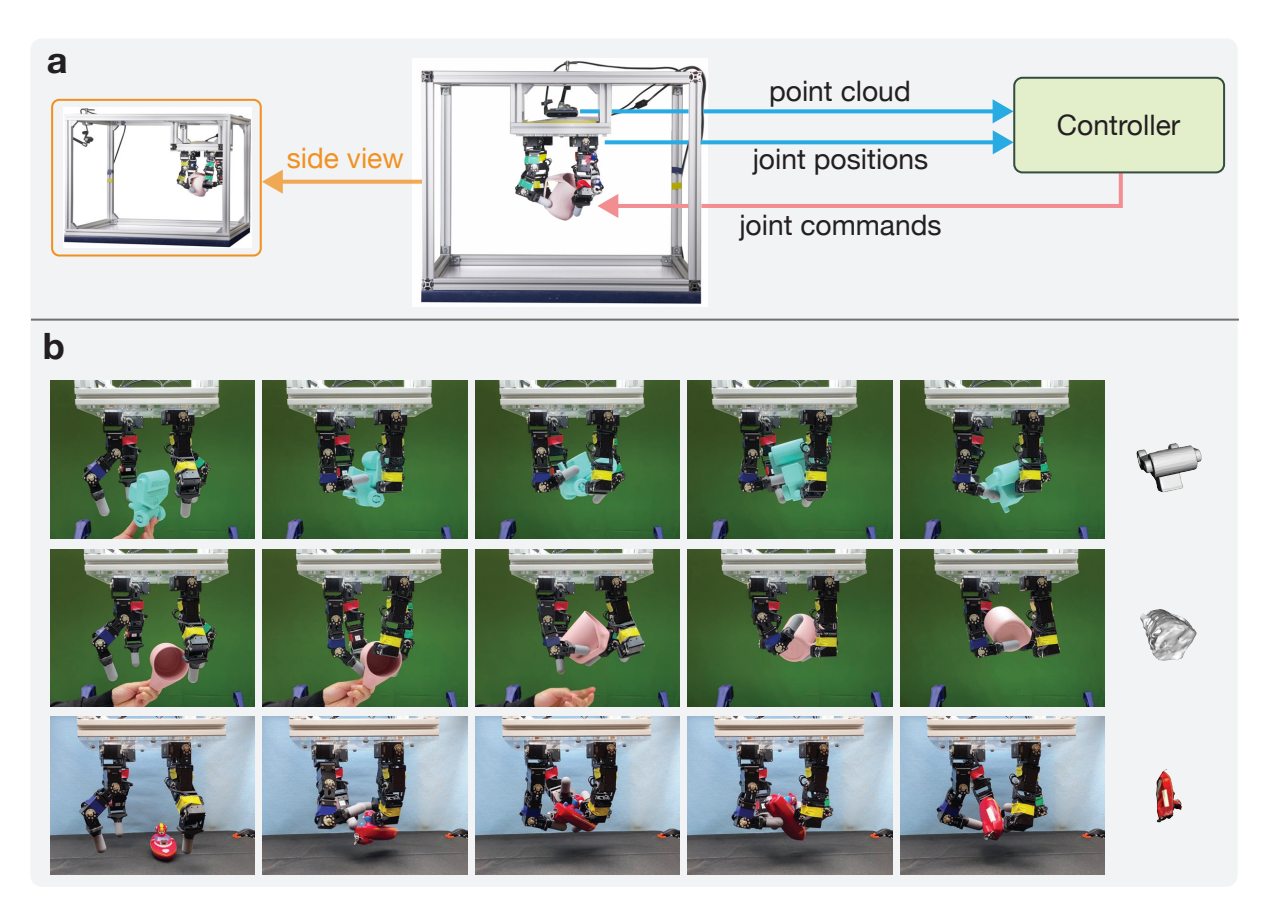


Fig. 1 (a): the front and side views of our real-world setup. The controller is a neural network that uses depth recordings from a single camera along with the joint positions of the manipulator to predict the change in joint positions. (b): Visualization of the same controller reorienting three different objects. The rightmost column shows the target orientation. The first two rows are instances of a four-fingered hand reorienting objects in the air. The last row shows reorientation with the help of a supporting surface (i.e., extrinsic dexterity).

initial configuration of the object is a random transformation in SE(3) space within the range of the robot's fingers – either the object is set on a table or handed over by a human to the robot.

We experiment with the hand in the downward-facing configuration in two settings: with and without a supporting table. Our system runs in real-time at a control frequency of 12Hz using a commodity workstation. Figure 1 shows intermediate steps of manipulating three objects to target orientations depicted in the rightmost column. The proposed controller successfully reorients a diverse set of *novel* objects with complex geometries that were not used for train-

ing. Movie S1 visualizes the videos of object reorientation and summarizes our major findings. Movie S2 visualizes the robot's behavior when reorienting objects in a sequence of target orientations. To quantitatively measure the orientation error, we use an OptiTrack motion capture system to track object pose. We define error as the distance between the goal orientation and the object orientation when the controller predicts it has reached the target configuration and stops. The motion capture is only used for evaluation and is not required by our controller otherwise.

For quantitative evaluation, we use seven objects from the training dataset (\mathbb{B}), which we refer to as *in-distribution*, and five objects from the held-out test dataset (\mathbb{S}), which we refer to as *out-of-distribution* (OOD). Objects are shown in Figure 3a. We test each object 20 times with random initial and goal orientation in each testing condition. We 3D print these objects to ensure the shape of objects in simulation and the real world is identical, which is helpful in evaluating the extent of *sim-to-real* transfer. While the shape of these seven objects is included in the training set, the surface properties such as friction of the real-world objects, may not correspond to any object used for training in simulation. Evaluation on five OOD objects tests generalization to shapes. To further showcase generalization to shapes and different material properties, we also present results on some rigid objects that humans encounter in daily life.

Extrinsic dexterity: object reorientation with a supporting surface

We first report results on the easier problem of reorienting objects when the table is present below the hand to support the object. Using an external surface to aid reorientation has been referred to as *extrinsic dexterity* (34) and is necessary in many real-world use cases. Visualization of the proposed controller reorienting a diverse set of objects is provided in Figure 2. To demonstrate the versatility of our system, we present results of the robot manipulating objects of different shapes, materials, surfaces, fingertip materials and varying number of fingers.

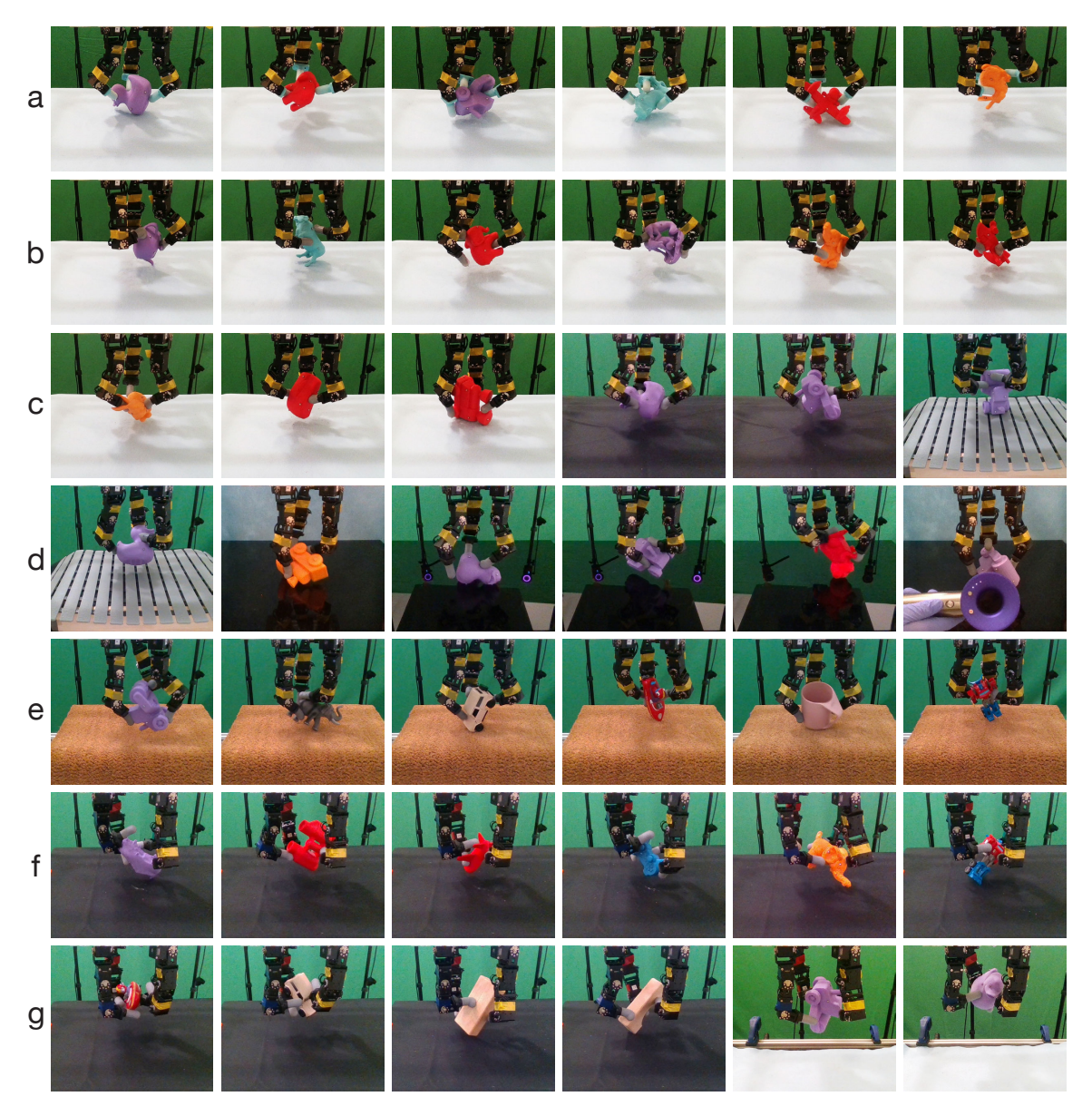


Fig. 2 We test our controller on objects with diverse shapes and reorientation conditions such as using different supporting surfaces: a tablecloth, an *uneven* door mat, an *slippery* acrylic sheet, a *perforated* bath mat, etc. We also evaluate performance using fingertips with different softness: rigid 3D-printed (row (a)), and soft elastomer fingertips (rows (b) to (g)). Row (a) to (e) use a *three-fingered* robot hand. And row (f) to (g) use a *four-fingered* robot hand. Our policy can reorient real household objects (rows (e,g)) and can operate without the need for a supporting surface (i.e., in the air) as shown in row (g).

Reorientation using a three-fingered manipulator with rigid and soft fingertips

With table support, three fingers are sufficient for the reorientation task. The error distribution for different objects, when tested on a table surface covered with a white cloth (material M1 in Figure 3e), is shown in Figure 3b using a violin plot (36). While the overall error distribution is more informative, for ease of comparison, in Table 1 we report summary statistics of success rate measured as the percentage of tests error was within 0.4 or 0.8 radians. The seven train objects can be reoriented successfully within an error of 0.4 radians 81% of the time. Performance on the five OOD test objects is lower with a success rate of 45%. As expected, the performance is much better with a relaxed error threshold of 0.8 rad.

Qualitatively observing the robot behavior revealed that one cause of failures was object overshooting the target orientation or the finger slipping across the object, especially for OOD objects. One explanation is that because we used *rigid* hemispherical fingertips, whose contact area with the object is very small (i.e., close to making point contact), it makes small errors in action commands more pronounced. Further, we found that the fingertip material had low friction resulting in slips which made manipulation harder. To mitigate these issues, we designed and fabricated soft fingertips that cover the rigid 3D-printed skeleton with a soft elastomer (see Figure S2c). Soft fingertips provide higher friction and deform when contact happens (i.e., compliance), increasing the contact area between the finger and the object. The error distribution in Figure 3c shows that the use of soft fingers doesn't affect performance on train objects but improves generalization to OOD objects. Results in Table 1 confirm the findings – success rate on OOD objects increases from 45% to 55% when switching from rigid to soft fingertips. We noticed that soft fingertips behave less aggressively compared to rigid fingertips resulting in smoother object motion. We, therefore, use soft fingertips in the rest of the experiments. It's worth noting that although the controller was trained using a rigid-body simulator, it successfully transfers to soft fingertips in the real world, demonstrating the robustness of our controller.

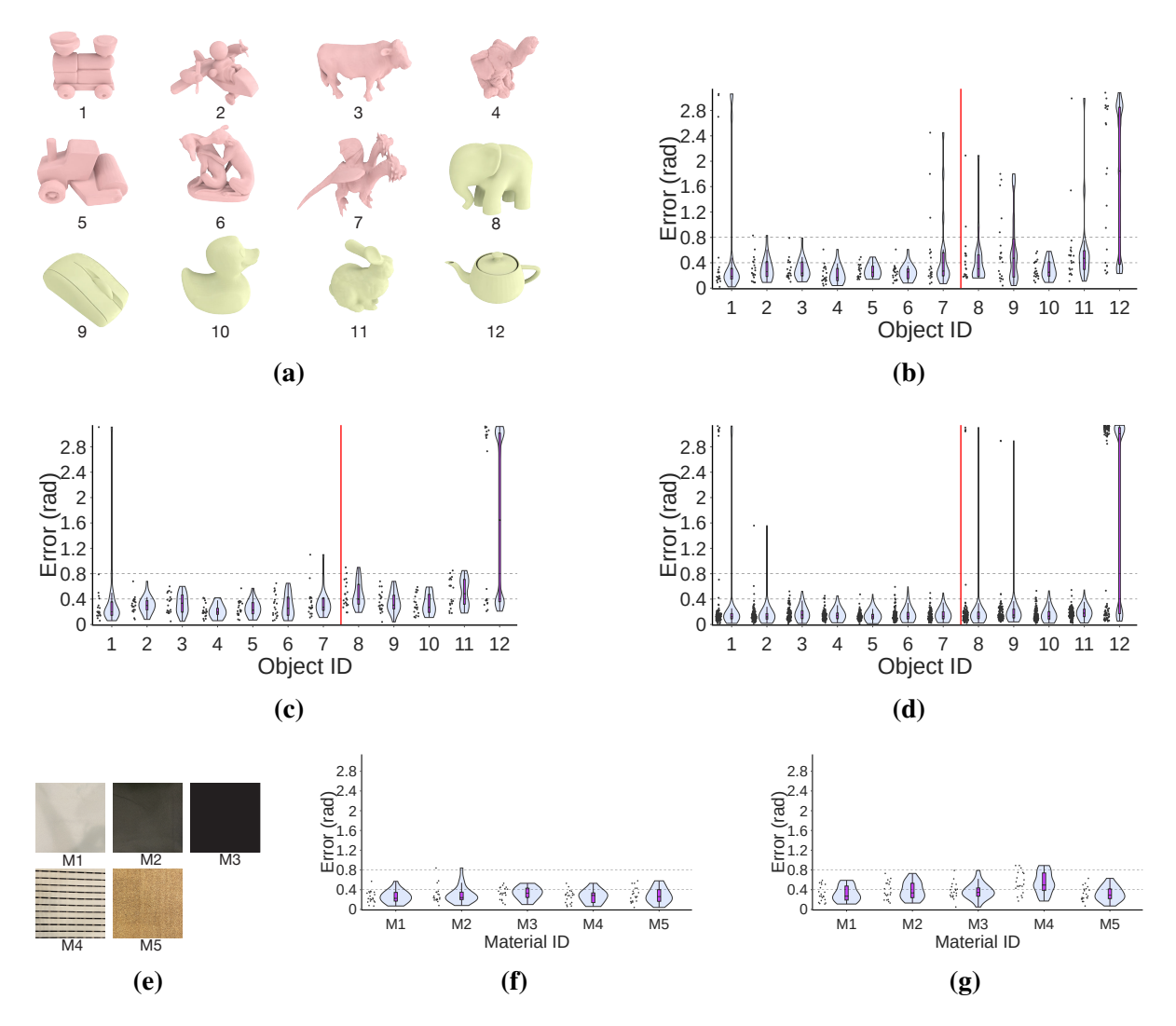


Fig. 3 (a): twelve objects with their IDs. The first seven objects are from the training dataset \mathbb{B} , and the last five are from the testing dataset \mathbb{S} . (b), (c) show the *real-world* error distribution when using rigid and soft fingertips, respectively, on material M1. (d) shows the error distribution *in simulation* for each object as a *violin* plot (36). The violet rectangle shows the errors within [25%, 75%] percentile and the horizontal bar in the rectangle depicts the median error. Train objects can mostly be reoriented within an error of 0.4rad, with similar performance for rigid and soft fingertips. The error on test objects is higher, and soft fingertips exhibit better generalization. (e): five table materials. (f) and (g) show the error distribution on different materials for object #5 and #10, respectively.

The reorientation error can result from imperfect training, *sim-to-real* gap, generalization gap, or failures at detecting if the object is at the target orientation, which triggers the controller

Table 1: Statistics of the orientation error when the hand reorients objects on a table. **CI** stands for bias-corrected and accelerated (BCa) bootstrap confidence interval. **Train** stands for testing on the seven objects (Figure 3a) from the training dataset \mathbb{B} . **Test** stands for testing on the five objects from the testing dataset \mathbb{S} .

	with rigid fingertips (real)		with soft fingertips (real)		in simulation	
	Train	Test	Train	Test	Train	Test
$\leq 0.4 \text{rad} (22.9^{\circ})$	81%	45%	79%	55%	96%	85%
95% C I	[73%, 90%]	[32%, 58%]	[71%, 86%]	[44%, 62%]	[94%, 97%]	[82%, 88%]
$\leq 0.8 \text{rad} (45.8^{\circ})$	95%	75%	98%	86%	98%	87%
95% CI	[88%, 98%]	[46%, 91%]	[96%, 99%]	[58%, 96%]	[97%, 99%]	[84%, 90%]
95% CI of the median of orientation errors (rad)	[0.20, 0.27]	[0.29, 0.46]	[0.21, 0.28]	[0.33, 0.42]	[0.12, 0.13]	[0.15, 0.18]

to stop. In Figure 3d, we report the error distribution in simulation. While the trained controller is not perfect in simulation, the errors in simulation follow the same trend as in the real world (Figure 3c) but are lower, indicating some sim-to-real gap. As shown in Table 1, the sim-to-real gap is insignificant with a relaxed error threshold of 0.8rad than with a threshold of 0.4rad, illustrating the difficulty in precise reorientation. For some objects (e.g., #1, #12), the error distribution is bi-modal both in simulation and the real world. The test runs with high errors largely result from incorrect detection of when to stop. For instance, object #12 appears nearly symmetric in the point cloud representation, which often leads to errors close to 180° . While it is hard to quantitatively disentangle errors caused by *sim-to-real* gap between action prediction and stopping criterion, based on our experience with the system, we hypothesize that the latter contributes more.

Object reorientation on different supporting materials

Changing the table surface results changes the dynamics of object motion. We tested if our controller is robust to a diverse set of materials: a rough cloth (M1), a smooth cloth (M2), a *slippery* acrylic sheet (M3), a bathtub mat with perforations resulting in *non-stationary object dynamics* depending on the object's position on the mat (M4), and a door mat with *uneven*

texture (M5). The materials have different surface structures, roughness, and friction, leading to different system dynamics. We evaluate with one in-distribution object (object #5) and one out-of-distribution object (object #10). Figure 3f and Figure 3g show that our controller performs well on different supporting materials.

Towards object reorientation in air

As the controllers discussed above were trained with a supporting surface, when the supporting surface was removed, the manipulator consistently dropped the object resulting in failures. Prior work used a specialized training procedure of configuring the object in a good pose at the start of each training episode and a manually designed gravity curriculum (7) to learn in-air (i.e., without supporting surface) reorientation controllers. Consequently, it was necessary to train separate controllers for reorientation with a supporting surface and in the air. It is preferable to have a single controller capable of in-air reorientation and use the supporting surface if available to recover from any dropping failures. We achieved this desideratum by employing a *four-fingered* hand and designing a reward function that penalizes contact between the object and the supporting surface to discourage the controller from using external support for reorientation. When the controller is trained on a supporting surface with the proposed reward function, in-air reorientation *emerges*.

While both three and four-fingered hands can reorient objects on a supporting surface (Figure 4a), only the four-fingered hand is successful at in-air reorientation (Figure 4b). We hypothesize this to be the case because, with four fingers, there are more ways of reorienting the object, making it easier for policy optimization to find one solution. Furthermore, the redundancy in the number of fingers makes the system more robust to errors in action prediction. For instance, an incorrect motion of two fingers in a three-fingered hand will almost surely lead to the object being dropped. However, with a four-fingered hand, the remaining two fingers may stabilize

the object preventing a catastrophic failure.

SO(3) object reorientation in air

The controller trained in simulation is able to reorient diverse real-world objects in the air, as shown in Figure 1b. In-air reorientation can fail if the object is not accurately reoriented or if the robot drops the object. Because in-air reorientation is more challenging, it is possible that the controller is less accurate at reorienting objects. We found the distribution of orientation error in trials where the objects are not dropped (Figure 4c) to be similar to reorientation with the supporting surface, indicating that the controller doesn't lose reorientation precision in the more challenging in-air scenario. In simulation analysis, we did not notice any significant correlation between orientation error and the distance between the initial and target orientations (Figure S7b), indicating that the controller succeeds at reorientation in the full SO(3) space.

Simulation analysis reveals that object dropping is the most significant source of errors (Figure S7c). Dropping rates vary substantially across objects. Real-world results follow the same trend. The dropping rate of a truck-shaped object (#5) was 23%, significantly lower than the dropping rate of 56% for an out-of-distribution duck-shaped object (#10). The dropping rate for the same object shape in the simulation was around 20% showing a sim-to-real gap. However, it remains unclear if the difference in performance can be attributed to the simulator being an approximate model of the real world or whether the object in the real world is much harder to manipulate. This is because, even though the simulation and real-world experiments used the object with the same shape, properties such as surface friction that are critical in reorientation can be difference. If an object is curved and has a smooth surface, which is the case with the duck, small differences in friction can substantially change the task difficulty. We chose to report results on the duck as it was among the harder objects to reorient and therefore highlights the limitations of our controller.

If a table is present below the hand (e.g., the setup shown in the third row of Figure 1b) and the object is dropped, we notice that our controller picks the object and continues reorienting – an instance of recovery from failures. It was possible that the reward term that encouraged in-air reorientation hurts on-table reorientation. However, the error distribution for on-table reorientation with the updated reward function (Figure 4e) is similar to earlier on-table experiments. Moreover, although our controller is trained using objects with asymmetry or reflective symmetry, which makes learning much easier, it generalizes reasonably well to symmetric objects (Figure 4f, more discussions in Section S5.1). The in-air, on-table, and dropping recovery results together demonstrate success in building a single controller that works across different scenarios.

Our controller performs dynamic reorientation, and the median time for successful manipulation across objects and randomly sampled orientation distances in the full SO(3) space is less than 7s (Figure 4d), which makes it the fastest in-air reorientation controller operating in the full SO(3) space. The reorientation times in the real world are longer than in simulation, which we believe results from contact dynamics in the real world being different from simulation.

Generalization to objects in daily life

In experiments reported until now, we used 3D-printed objects for the purpose of quantitative evaluation. Objects in the real world have different object dynamics due to differences in material properties that may also be variable across the object surface, non-uniform mass distribution, etc. To demonstrate the generalization of our controller to such objects, we performed a qualitative evaluation on objects taken from households. Because we don't have access to the CAD model of these objects to generate the point clouds in target orientations, we used a free and off-the-shelf iPad App called *Scaniverse* to scan the objects. Note that such a scan is only required to specify the target orientation. The scanned object cloud is imperfect (see Figure 5),

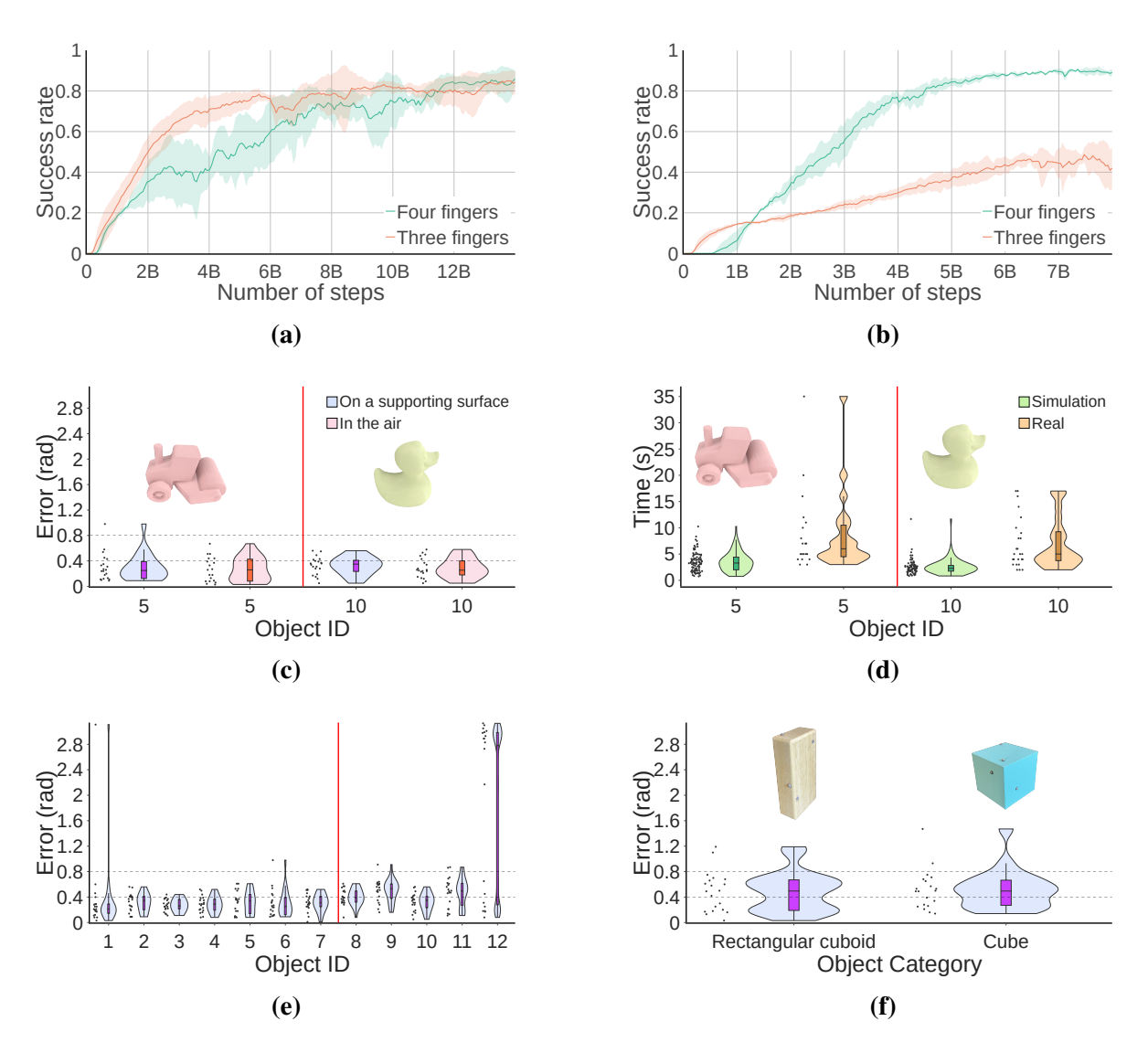


Fig. 4 (a): When training a controller to reorient objects with a supporting surface, the three-fingered and four-fingered hands achieve similar learning performance. (b): However, when we incentivize the hands to lift the object during reorientation, the four-fingered hand outperforms the three-fingered hand substantially. (c): We tested the controller performance with a four-fingered hand in the air. We collected 20 non-dropping testing cases for one in-distribution object and one out-of-distribution object. The error distribution is similar to that in the case of table-top reorientation. (d) shows the distribution of the episode time both in simulation and the real world. (e): We show the same controller's performance on twelve objects with a supporting surface. (f): We tested the controller on symmetric objects with a supporting surface. The controller behaves reasonably well even though it was never trained with symmetric objects.



Fig. 5 Examples of reorienting real objects that were not 3D printed using a four-fingered (top three rows) and a three-fingered (bottom four rows) manipulator.

resulting in the goal specification being noisy. Nonetheless, our controller is able to reorient these objects (see Figure 1b, Figure 5). The results demonstrate the robustness of our controller to noise in goal specification and generalization to new materials and shapes.

Discussion

Solving contact-rich tasks requires optimizing the location at which the robotic manipulator makes contact with the object. One would assume predicting the contact location requires

knowledge of the object's shape. However, inputs to the teacher policy have no information about object shape, yet it is able to successfully reorient diverse and novel objects. One might assume that the agent can gather shape information by the sequence of touches made by the fingers. But, the teacher policy is not recurrent, ruling out this possibility. The surprising observation of reorientation without knowledge of shape was made by earlier work in the context of a reorientation system that operates in simulation (7). However, because real-world results were not demonstrated, it remained unclear if such an observation was an artifact of the simulator or the property of the reorientation problem. With the successful sim-to-real transfer, we can say with more confidence that shape information may not be as critical to object reorientation as one might apriori think. However, this is not to suggest that shape is not useful at all. The results show that one can go quite far without shape information, but the performance can likely be improved by incorporating shape features, an exciting direction for future research.

One hypothesis about why we can get away with little shape information is that the hand is *over-parameterized* in the number of fingers. At least two fingers are required to grasp the object stably (i.e., maintain force closure). With a third finger, it is possible to reorient the object, but the number of possible ways of performing reorientation is limited. With more fingers, our hypothesis is that there is a larger number of finger configurations that can achieve the same reorientation. In such a situation, reliance on object shape might reduce.

Typically having a larger number of fingers introduces more optimization variables, making the optimization problem harder in the conventional view. However, we found some evidence to the contrary – having more fingers can make it *easier* for deep reinforcement learning to find a solution, especially in the challenging manipulation scenarios (in the air), analogous to overparameterized deep networks finding better solutions. The conjecture is that over-parameterized hardware results in a larger pool of good solutions, making it easier for current optimizers in deep learning to stumble upon a good solution.

A majority of prior real-world demonstrations of object reorientation achieved continuous reorientation where the robot was never tasked to stop and hold the object at the target orientation (8–10, 18, 26). When it comes to real-world applications, a robot hand needs to reorient the object, such as a tool, to proper orientation and hold it for downstream use. In practice, we found that, compared to continuous reorientation, it is harder to decelerate the dynamically moving object and transit it into a stable static goal orientation. While in continuous reorientation, the object's momentum can be leveraged, when the agent is tasked to stop and re-start manipulation, it needs to overcome the object's inertia. Further, the controller needs to identify when the goal orientation is reached, slow down the motion, and stably hold the object. To achieve this, we found it necessary to have the controller predict the orientation distance and design success criteria that explicitly encourage the robot hand to slow down object motion when it is close to the goal orientation.

In designing the proposed system, we either devised or made several technical choices: two-stage student training, representing both the camera recordings and proprioceptive readings as a point cloud, sparse convolution neural network for real-time control, use of limited domain randomization due to system identification, the method of system identification using parallel GPU simulation, use of soft material on fingertips, using a larger number of fingers instead of the conventional wisdom of using fewer fingers, etc. These choices, however, are not specific to in-hand reorientation but can be applied to a broad spectrum of vision-based manipulation of rigid bodies. We hope that the knowledge of these choices, along with a low-cost platform, can further the goal of democratizing research in dexterous manipulation.

Limitations and Possible Extensions Object reorientation with a downward-facing hand has significant room for improvement. One possible cause for dropping objects is that the control frequency of 12Hz is not fast enough. The robot dynamically manipulates the object, and it takes

a fraction of a second to lose control. Feedback control at a higher frequency may mitigate such failures. Achieving higher frequencies will require either more efficient neural network architectures or more processing power.

Another hypothesis is that the hand drops objects because the controller does not know when the finger is in contact with the object, if the object is slipping or how much force is being applied to the object. We conjecture that explicit knowledge of contact, contact force, and other signals such as slip will go a long way in improving the success rate of our system. Our agent currently relies purely on occluded vision sensing to infer contacts. Incorporating touch sensors on fingertips to overcome this limitation is an exciting direction for future investigation.

We used D'Claw manipulators in this work as it is open-source and low-cost. However, many aspects of the D'Claw setup, such as the design of fingers, and the number of fingers, are sub-optimal. For instance, while the performance of our manipulator is robust to the softness of fingertips, different softness and skeleton designs can significantly affect the longevity of fingertips. We manually iterated over many soft fingertip designs, which was time-consuming. Similarly, the fingertips have a hemispherical shape, quite different from humans and presumably not optimal. The performance of the task can be improved by better hardware design: the shape of fingers, the degrees of actuation on each finger, the placement of fingers, the choice of materials, etc. Manually iterating over these choices is infeasible. A promising future direction is to utilize a computational approach for automatically designing the hand for specific tasks (37).

While we achieve significant sim-to-real transfer, there remains room for improvement. How to further close the sim-to-real gap is a worthwhile direction for future research. Lastly, the performance of our policy on test objects is worse than on training objects. While we train controllers with 150 geometrically different objects, it is worth studying in the future if the generalization gap can be closed by training on more objects (e.g., thousands).

Materials and Method

Given a random object in a random initial pose, the robot is tasked to reorient the object to a user-provided target orientation in SO(3) space. We train a single vision-based object reorientation controller (or policy) in simulation to reorient hundreds of objects. The controller trained in simulation is directly deployed in the real world (i.e., zero-shot transfer). The choices in our experimental setup have been made to support future deployment of reorientation in service of tool use and on a mobile manipulator.

Object datasets We use two object datasets in this work: **Big dataset** (\mathbb{B}) and **Small dataset** (\mathbb{S}). \mathbb{B} contains 150 objects from internet sources. \mathbb{S} contains 12 objects from the ContactDB (38) dataset. These two datasets do not have overlapped shapes. More details on the object dataset are in Section S2.1.

Simulation setup We use Isaac Gym (39) as the rigid body physics simulator. We train all the policies on a table-top setup (as shown in Figure 7a): hands face downward with a supporting table.

Success criteria The success criterion defines when the agent has accurately reoriented the object in the target configuration. Its purpose is two-fold: a reward signal during training and a criterion that signals success to stop the reorientation policy and thereby end the episode during training. A straightforward success criterion is judging whether an object's orientation is close to the target orientation (*orientation criterion*). The controller learned using the criterion when evaluated in simulation results in a behavior wherein the robotic fingers stabilize the object when its orientation is close to the target. However, the same controller, when evaluated in the real world, often does not result in fingers stopping when the object orientation is close

to the target leading to overshooting. Consequently, instead of stopping, the object oscillates around the target orientation. We believe this is a result of sim-to-real gaps, including the control latency, observation noise, and the difference in dynamics, etc. We ameliorate this issue by expanding the definition of success criterion to penalize finger and object motions explicitly. The task is considered completed successfully in the simulation if all the following three criteria are satisfied:

- Orientation Criterion is satisfied when $|\Delta \theta_t| < \bar{\theta}$ where $\Delta \theta_t$ is the distance between the object's current and target orientation.
- Finger motion criterion requires the joint motion of the robot to be small and is satisfied when $||\dot{q}_t|| < \bar{q}$ and $||a_t|| < \bar{a}$ where \dot{q}_t is the joint velocities at time step t, a_t is the policy output.
- Object motion criterion requires the object's velocity to be small. It is satisfied when $||v_t^o|| < \bar{v}$ and $||\omega_t^o|| < \bar{\omega}$ where v_t^o, ω_t^o denote object's linear and angular velocities respectively.

 $\bar{\theta}, \bar{q}, \bar{a}, \bar{v}, \bar{\omega}$ are manually defined thresholds. The finger and object motion criteria act as regularizers to explicitly encourage the policies to slow down the motion near the end.

Training the visuomotor policy

We model the problem of learning the controller, π , as a finite-horizon discrete-time decision process with horizon length T. The policy π takes as input sensory observations (o_t) and outputs action commands (o_t) at every time step t. Learning π using RL is data inefficient when the observation (o_t) is high-dimensional (e.g., point clouds). The reason is that the policy needs to simultaneously learn which features to extract from visual observations and what are the high-rewarding actions. The problem would be simplified if one of these factors were known: learning a policy via RL from sufficient state information would be much easier than direct

learning from sensory observations. Similarly, apriori knowledge of high-rewarding actions would reduce the data requirements of learning from visual observations.

Prior work has employed this intuition to ease policy learning by decomposing the learning process into two steps (7, 28, 29, 31). In the first step, a *teacher* policy is trained in simulation with RL using low-dimensional state space that includes *privileged* information. In the case of in-hand object reorientation, privileged information includes quantities such as fingertip velocity, object pose, and object velocity that can be directly accessed from the simulator but can be challenging to measure in the real world. Because the teacher policy operates from a low-dimensional state space, it can be more efficiently trained using RL. Next, to enable operation in the real world, one can either train a perception system to predict the privileged information (8, 27) or train a second *student* policy to predict high-rewarding teacher actions from raw sensory observations via supervised learning (7, 28, 29, 31).

An underlying assumption of the two-stage training paradigm is that a low-dimensional state for learning a *teacher* policy can be identified. Because there are no tools available to theoretically analyze if a particular choice of state space is sufficient for policy learning, selecting the state inputs for the *teacher* policy is a manual process based on human intuition. At first, object reorientation might seem to require knowledge of object shape since the controller must reason about where to make contact. If object shape is necessary, then it will not be possible to reduce depth observations into a low-dimensional state. However, past work found that even without any shape information, it is possible to train RL policies to achieve good reorientation performance on a diverse set of objects in simulation (7). Therefore, teacher-student training can be leveraged to simplify the learning of object reorientation.

To deploy the policy in the real world, some prior works train a perception system to predict the object pose (8,9). However, object pose is only defined with respect to a particular reference frame. Choosing a common frame of reference across different objects is not possible. As a

consequence, pose estimators cannot generalize across objects. Therefore, we choose to train an end-to-end *student* policy that takes as input the raw sensory observations and is optimized to match the actions predicted by the *teacher* policy via supervised learning (DAGGER; (40)). Because supervised learning is considerably more data efficient than RL, such an approach solves the hard problem of learning a policy from raw sensory observations.

The *teacher-student* training paradigm has been used to learn object reorientation policy in simulation from visual and proprioceptive observations (7). However, a separate policy was trained per object. Secondly, it required more than a week to train the student vision policy for a single object on an NVIDIA V100 GPU. We developed a novel two-stage student training (Teacher-student²) framework that substantially speeds up the vision student policy learning. Using this framework, we were able to learn a vision policy that operates across a diverse set of objects and generalizes to objects with novel shapes and physical parameters.

Teacher policy: reinforcement learning with privileged information

The learning of teacher policy $(\pi^{\mathcal{E}})$ is formulated as a reinforcement learning problem where the robot observes the current observation $(o_t^{\mathcal{E}})$, takes an action (a_t) , and receives a reward (r_t) afterward. A single policy $(\pi^{\mathcal{E}})$ is trained across multiple objects using PPO (41) to maximize the expected discounted episodic return: $\pi^{\mathcal{E}^*} = \arg\max_{\pi^{\mathcal{E}}} \mathbb{E}\left[\sum_{t=0}^{T-1} \gamma^t r_t\right]$. Since the observation o_t at a single time step t does not convey the full state information such as the geometric shape of an object, our setup is an instance of *Partially Observable Markov Decision Process* (POMDP). However, for the sake of simplicity and based on the finding that knowledge of object shape may not be critical as discussed above, we chose to model the policy as a *Markov Decision Process* (MDP): $a_t = \pi^{\mathcal{E}^*}(o_t; a_{t-1})$. The policy also takes as input the previous action (a_{t-1}) to encourage smooth control.

Observation space The inputs to the teacher policy, o_t , include proprioceptive state information, object state, and target orientation. Details are shown in Section S2.2.

Action space We use position controllers to actuate the robot joints at a frequency of 12Hz. The policy outputs the relative joint position changes $a_t \in \mathbb{R}^{3G}$. Instead of directly using a_t , we use the *exponential moving average* of actions $\bar{a}_t = \alpha a_t + (1 - \alpha)\bar{a}_{t-1}$ for smooth control, where $\alpha \in [0,1]$ is a smoothing coefficient. In our experiments, we set $\alpha = 0.8$. Given the smoothed action \bar{a}_t , the target joint position at the next time step is: $q_{t+1}^{tgt} = q_t + \bar{a}_t$.

Reward We first describe the reward function for the hand to reorient objects on a table. The first term in the reward function (Equation 1) is the success criteria for the task. However, since this only provides sparse reward supervision, the criteria by itself is insufficient for successful learning. Therefore we add additional reward shaping (42) terms to encourage reorientation. We use a dense reward term that encourages minimization of the distance $(\Delta \theta_t)$ between the agent's current and target orientation (Equation 2). We penalize the agent for moving fingertips far away from the object (Equation 3). Without this term, fingers barely made any contact with the object during training. We also penalize the agent for expending energy (Equation 4) and for pushing the object too far from the robot's hand (Equation 5) in which case the episode is also terminated. The reward terms are mathematically expressed as:

$$r_{1t} = c_1 \mathbb{1} \text{ (Task successful)}$$
 sparse task reward (1)

$$+c_2 \frac{1}{|\Delta \theta_t| + \epsilon_\theta}$$
 dense task reward (2)

$$+c_3 \sum_{i=1}^{G} \left\| \boldsymbol{p}_t^{f_i} - \boldsymbol{p}_t^o \right\|_2^2$$
 keep fingertip close to the object (3)

$$+c_4|\dot{\boldsymbol{q}}_t|^T|\boldsymbol{\tau}_t|$$
 energy reward (4)

$$+c_5\mathbb{1}(\|\boldsymbol{p}_t^o\|_2^2 > \bar{p})$$
 penalty for pushing the object away (5)

where $c_1, c_2 > 0$, and $c_3, c_4, c_5 < 0$ are coefficients, 1 is an indicator function, ϵ_{θ} and \bar{p} are constants, $p_t^{f_i}$ is the fingertip position of i^{th} finger, p_t^o is the object center position, τ_t is the vector of the joint torques.

Using the aforementioned reward function, we were able to successfully train reorientation policies that used the support of the table. Next, to enable the more challenging behavior of reorienting objects in the air, we added: (1) penalty for the contact between the object and table (Equation 7) and (2) penalty for using the penultimate joint instead of the fingertip for reorientation (Equation 8). While the term in Equation 8 is not critical, it results in more natural looking behaviors. The overall reward function is:

$$r_{2t} = r_{1t} \tag{6}$$

$$+c_6\mathbb{1}$$
 (object contacts with the table) (7)

$$+c_7 \sum_{i=1}^{N} \mathbb{1}(p_{t,z}^{f_i} > \bar{p}_z) \tag{8}$$

where $c_6, c_7 < 0$ are coefficients.

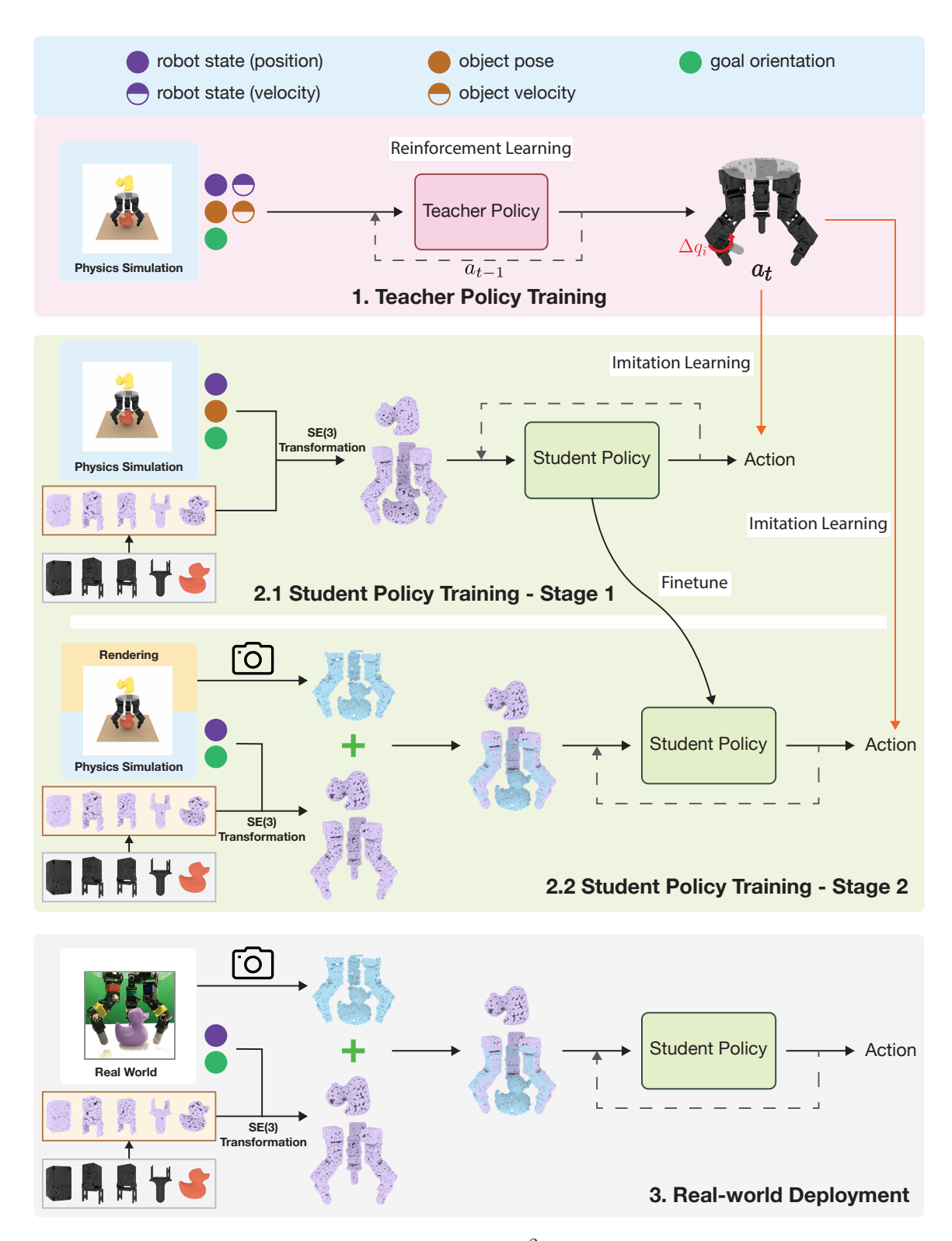


Fig. 6 Teacher-student² framework

Student policy - imitation learning from depth observations

The student policy (π^S) is trained in simulation with the purpose of being deployed in the real world. Since the sim-to-real gap for depth data is less pronounced than RGB data, we only use the depth images provided by the camera along with readings from joint encoders. We represent the depth data as a point cloud in the robot's base link frame. To enable the neural network representing π^S to model the spatial relationship between the fingers and the object, we express the robot's current configuration by showing the policy a point cloud representing points sampled on the surface of the fingers. We concatenate the point cloud obtained from the camera along with the generated point cloud of the hand. We denote this scene point cloud as P_t^s .

Goal representation Instead of providing the goal orientation as a pose which has generalization issues discussed above, the goal is represented as the object's point cloud in the target orientation P^g . In other words, the policy sees how the object should look in the end (see the top left of Figure 7a).

Observation space The input to π^S is the point cloud $P_t = P_t^s \cup P^g$ (see Figure 7a). We also did an ablation study on different ways to process the goal point cloud in Section S5.2. The results show that merging P_t^s and P^g before they are input to the network leads to faster learning.

Architecture The critical requirement for the vision policy is to run at a high enough frequency to enable real-time control. For fast computation, we designed a sparse convolutional neural network to process point cloud (P_t) using the Minkowski Engine (43) (see Figure 7a). Compared to the architecture used in (7), our convolutional network has a higher capacity to

make it possible to learn the reorientation of multiple objects. Without direct access to object velocity, it is necessary to integrate temporal information in π^{S} , for which we use the gated recurrent unit (GRU; (44)) in the network.

Optimization The student policy $\pi^{\mathcal{S}}$ is trained using DAGGER (40) to imitate the teacher policy $\pi^{\mathcal{E}}$.

Need for two-stage student learning We found training a vision policy in simulation to be slow, consuming 20+ days on an NVIDIA V100 GPU (Figure 7c). The main reason for slow training is that the simulator performs rendering to generate a point cloud which consumes a substantial amount of time and GPU memory. To reduce training time, we generated synthetic point clouds by uniformly sampling points on the object and robot meshes used by the simulator. The synthetic point cloud is also complete (i.e., no occlusions), which makes training easier. The vision policy (π_1^S) can be trained with *synthetic point cloud* in less than three days, i.e., $7 \times$ speedup (stage 1; see Figure 7c). However, the policy, $\pi_1^{\mathcal{S}}$, cannot be deployed in the real world because it operates on an idealized point cloud (i.e., no occlusions). Therefore, once the student reaches high performance, we initiate stage 2, where the policy is finetuned with the rendered point cloud. Such finetuning is quick in wall-clock time (around one day), and the resulting policy (π_2^S) performs better than training from scratch with rendered point clouds (see Figure 7c). It is possible to further reduce the training time of the student policy by employing visual pre-training with passive data that we discuss in Section \$5.3. An additional benefit of the two-stage student policy training is that $\pi_1^{\mathcal{S}}$ is agnostic to the camera pose. Therefore a policy from a new viewpoint (π_2^S) can be quickly obtained by finetuning using rendered point clouds from that camera pose. Training the vision policy from scratch is not necessary.

Stage 1: details of synthetic point cloud In stage 1, the simulation is not used for rendering but only for physics simulation. We generate the point cloud for each link on the manipulator and object by sampling K points on their meshes in the following way: let the point cloud of link l_j in the local coordinate frame of the link be denoted as $\mathbf{P}^{l_j} \in \mathbb{R}^{K \times 3}$. Given link orientation $(\mathbf{R}^{l_j}_t \in \mathbb{R}^{3 \times 3})$ and position $(\mathbf{p}^{l_j}_t \in \mathbb{R}^{3 \times 1})$ at time step t, the point cloud can be computed in the global frame, $\mathbf{P}^{l_j}_t = \mathbf{P}^{l_j}(\mathbf{R}^{l_j}_t)^T + (\mathbf{p}^{l_j}_t)^T$. The point cloud representation of the entire scene is the union of point clouds of all the links, the object being manipulated, and the object in the goal orientation: $\mathbf{P}^s_t = \bigcup_{j=1}^{j=M} \mathbf{P}^{l_j}_t$ where M is the total number of links (bodies) in the environment. The point cloud \mathbf{P}^s_t can be efficiently generated using matrix multiplication.

Stage 2: details of rendered point cloud In stage 2, we acquire depth images from the simulator at each time step and convert the depth images to point clouds (which we call *exteroceptive point cloud*) using the camera's intrinsic and extrinsic matrices. Note that such a point cloud is not complete due to occlusions from a single camera. We also convert the joint angle information into link poses via forward kinematics and then generate the complete point cloud of the robot (which we call *proprioceptive point cloud*). Note that such a proprioceptive point cloud of a robot can be easily obtained in the real world in real-time as well since we can get the joint positions on the real robot. The policy input consists of the union of the exteroceptive point cloud and the proprioceptive point cloud.

Student policy closely tracks the performance of teacher policy

We evaluated our learned policies on the training object dataset (\mathbb{B}) and the testing object dataset (\mathbb{S}), respectively, in simulation. To characterize how well a policy behaves in the testing time, we use the empirical cumulative distribution function (ECDF) as the metric to measure the distribution of the errors ($\Delta\theta$). Figure 7d shows the ECDF curves for the teacher policy and student policies at stages 1 and 2, respectively. Using fully-observable low-dimensional state

information, the teacher policy achieves the highest success rate at any error threshold. The student policies are able to track the teacher policy's performance closely.

Overcoming the simulation to reality gap

There are two main sources of gap between simulation and reality. The first one is *dynamics* gap that arises from differences in the robot dynamics, the approximation in the simulator's contact model, and differences in object dynamics that depends on material properties such as friction, etc. The other source is *perception* gap caused by differences in statistics of sensor readings and/or noise. One way to overcome these gaps is to train a single policy across many different settings of the simulation parameters (i.e., domain randomization (33)). The success of domain randomization hinges on the hope that the real world can be well approximated by one of the many simulation parameter settings used during training. The chances that one of the parameter settings being used in simulation being close to the real world increases by randomizing parameters over a larger range. However, excessive randomization may result in an overly conservative policy with low performance (45). Therefore, we make design choices that reduce the need for domain randomization and use it only when needed.

The *perception* gap is reduced by using only depth readings from the camera which is represented as a point cloud and is sufficient for reorienting objects with different shapes. To account for noise in depth readings, we add noise to the simulated point cloud (Section S4.2.1). The *dynamics* gap can be reduced by identifying simulation parameters that are closest to the real world. While such identification is possible for the robotic manipulator, it is infeasible to do so for object dynamics that vary in material, mass distribution, etc. Therefore, we perform system identification on the robot dynamics and use only small randomization to account for unmodeled errors. We use larger range of domain randomization (Section S4.2.2) on the object and environment dynamics. To make the policy more robust to unmodeled real-world physics, we

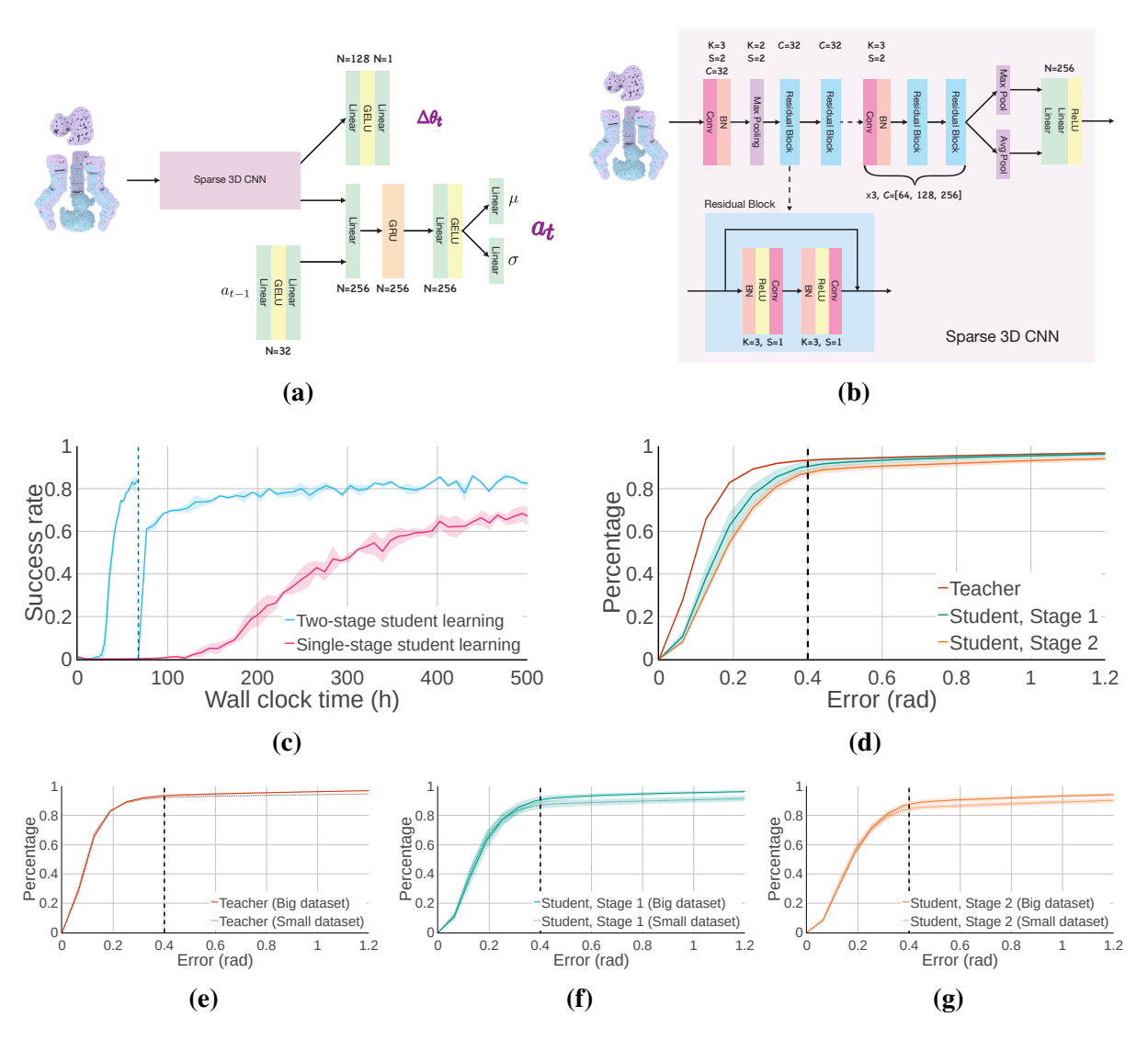


Fig. 7 (a): Student vision policy network architecture. (b): Sparse 3D CNN component of the policy network. (c): Proposed two-stage student learning learns faster than single-stage student learning. The dashed vertical line denotes the transition from the first to the second stage of student learning. The performance dip happens due to a change in the distribution of point cloud inputs from being unoccluded in the first stage to being occluded in the second. (d): Post-training evaluation of teacher and student policies on the training dataset \mathbb{B} . For each object, the initial and target orientations are randomly sampled 50 times, resulting in 7500 samples. The empirical cumulative distribution function (ECDF) of the orientation error is plotted. The results show that the students are close to the teacher's performance. (e), (f), (g): Comparing the ECDFs of the policies being evaluated on dataset \mathbb{B} and dataset \mathbb{S} reveals small generalization gap for all the policies.

apply random forces (Section S4.2.3) on the object during training which pressures the policy to reorient objects while being robust to external disturbance. Lastly, to increase compliance and friction between the object and the manipulator, we use soft fingertips. Such a choice makes the system more tolerant to errors in control commands. Empirically we noticed that soft fingertips make the robot less aggressive and result in fewer overshoots.

System identification of robot dynamics

We build the Unified Robot Description Format (URDF) models for the hands using their CAD models. While accurate kinematics parameters can be obtained from the CAD model, the dynamics parameters, such as joint damping and stiffness, must be estimated. One way of identifying dynamics parameters is to write down the equations of motion (or the dynamics model) and solve for the unknown variables using the collected robot's motion trajectories. The Isaac Gym simulator we use already has a built-in dynamics model. But because the simulator's code is not open-source, we do not have access to the precise dynamics model nor any access to gradients of dynamics parameters. We, therefore, propose to use a black-box approach that leverages the ability of Isaac Gym to perform massively parallel simulations. We spawn a large number of simulations with different dynamics parameters and use the one that has the closest match to the real robot's motion.

Let $\lambda_i \in \Lambda$ denote the dynamics parameter of the i^{th} simulated robot (C^{λ_i}) , where Λ denotes the entire set of dynamics parameter values over which search is performed. To evaluate similarity between the motion of C^{λ_i} and the real robot (C^{real}) , we compute the score: $h(q_A^{C^{real}}(\cdot), q_A^{C^{\lambda_i}}(\cdot)) = -\left\|q_A^{C^{real}}(\cdot) - q_A^{C^{\lambda_i}}(\cdot)\right\|_2^2$, where $q_A^C(\cdot)$ represents the joint position trajectories of a robot C given action commands $A(\cdot)$ which are detailed in Section S4.1. The closer is the motion of the simulated robot to the real-world, the higher is the score. We use the black-box optimization method of CMAES (46), an instance of evolutionary search algorithm,

to determine the optimal dynamics parameter: $\lambda^* = \arg\max_{\lambda \in \Lambda} h(q_A^{C^{real}}(\cdot), q_A^{C^{\lambda}}(\cdot))$. Note that it might be impossible to find a simulated robot that exactly matches the real robot due to approximate parameterization of real-world dynamics in simulation and the stochasticity in the real-world resulting from actuation/sensing noise. More details on the identification are in Section S4.1.

Real-world deployment

Real-world observation The observation consists of the joint positions of each motor in the robotic hand and the depth image from the RealSense camera. Details on how we convert the joint positions and depth image into a unified point cloud input can be found in Section S2.3.

Stopping criteria To automatically stop the robot, we train a predictor that re-uses features from the policy network to predict $|\Delta \theta_t|$ (see Figure 7a). We stop the robot when $\Delta \theta_t^{pred} < \bar{\theta}$ and $||a_t|| < \bar{a}$.

More details on how we come up with the stopping criteria, how we build the real-world setup, and how we perform the quantitative evaluation are in Section \$2.3.

Acknowledgments

We thank the members of the Improbable AI lab for the helpful discussions and feedback on the paper. We are grateful to MIT Supercloud and the Lincoln Laboratory Supercomputing Center for providing HPC resources.

Funding: Toyota Research Institute, DARPA Machine Common Sense, MIT-IBM Watson AI Lab, MIT-Airforce AI Accelerator provided funds to support this work. The views and conclusions contained in this document are those of the authors and should not be interpreted as representing the official policies, either expressed or implied, of the DARPA or the United

States Air Force or the U.S. Government. The U.S. Government is authorized to reproduce and distribute reprints for Government purposes notwithstanding any copyright notation herein.

Author contributions: T.C. and P.A. jointly conceived of the project. T.C. formulated the main idea of the training and control methods, set up the simulation and training code, trained the controllers, designed and built the real-world hardware platforms, developed the software for controlling the real hands, designed and conducted experiments in simulation and in the real world, and led the manuscript writing. M.T. designed and fabricated the fingertips of the robot hand, a majority of objects used for real-world evaluation and built the four-finger hand. S.W. experimented with vision network pre-training (Stage 0 in the paper) and performed ablations quantifying the effect of each pre-training task. V.K. provided feedback on the manuscript. E.A. provided advice and support for hardware fabrication. P.A. was responsible for overall project supervision, contributed to research discussions, provided advise on experimental design and setup, and played a substantial role in manuscript writing.

Competing interests: The authors declare that they have no competing interests.

Data and materials availability: All data needed to evaluate the conclusions in the paper are present in the paper or the Supplementary Materials. The code will be released after the acceptance.

References

- 1. M. T. Mason, J. K. Salisbury, and J. K. Parker, *Robot hands and the mechanics of manipulation*. The MIT Press, 1989.
- 2. J. K. Salisbury and J. J. Craig, "Articulated hands: Force control and kinematic issues," *The International journal of Robotics research*, vol. 1, no. 1, pp. 4–17, 1982.
- 3. D. Rus, "In-hand dexterous manipulation of piecewise-smooth 3-d objects," *The International Journal of Robotics Research*, vol. 18, no. 4, pp. 355–381, 1999.
- 4. I. Mordatch, Z. Popović, and E. Todorov, "Contact-invariant optimization for hand manipulation," in *Proceedings of the ACM SIGGRAPH/Eurographics symposium on computer animation*, 2012, pp. 137–144.
- 5. Y. Bai and C. K. Liu, "Dexterous manipulation using both palm and fingers," in 2014 IEEE International Conference on Robotics and Automation (ICRA). IEEE, 2014, pp. 1560–1565.
- 6. V. Kumar, Y. Tassa, T. Erez, and E. Todorov, "Real-time behaviour synthesis for dynamic hand-manipulation," in 2014 IEEE International Conference on Robotics and Automation (ICRA). IEEE, 2014, pp. 6808–6815.
- 7. T. Chen, J. Xu, and P. Agrawal, "A system for general in-hand object re-orientation," in *Conference on Robot Learning*. PMLR, 2021, pp. 297–307.
- 8. OpenAI, M. Andrychowicz, B. Baker, M. Chociej, R. Jozefowicz, B. McGrew, J. Pachocki, A. Petron, M. Plappert, G. Powell, A. Ray *et al.*, "Learning dexterous in-hand manipulation," *The International Journal of Robotics Research*, vol. 39, no. 1, pp. 3–20, 2020.

- 9. OpenAI, I. Akkaya, M. Andrychowicz, M. Chociej, M. Litwin, B. McGrew, A. Petron, A. Paino, M. Plappert, G. Powell, R. Ribas *et al.*, "Solving rubik's cube with a robot hand," *arXiv preprint arXiv:1910.07113*, 2019.
- 10. A. Nagabandi, K. Konolige, S. Levine, and V. Kumar, "Deep dynamics models for learning dexterous manipulation," in *Conference on Robot Learning*. PMLR, 2020, pp. 1101–1112.
- D. Bertsimas and J. N. Tsitsiklis, *Introduction to linear optimization*. Athena Scientific Belmont, MA, 1997, vol. 6.
- 12. N. Furukawa, A. Namiki, S. Taku, and M. Ishikawa, "Dynamic regrasping using a high-speed multifingered hand and a high-speed vision system," in *Proceedings 2006 IEEE International Conference on Robotics and Automation, 2006. ICRA 2006.* IEEE, 2006, pp. 181–187.
- 13. T. Ishihara, A. Namiki, M. Ishikawa, and M. Shimojo, "Dynamic pen spinning using a high-speed multifingered hand with high-speed tactile sensor," in *6th IEEE-RAS International Conference on Humanoid Robots*. IEEE, 2006, pp. 258–263.
- 14. V. Kumar, A. Gupta, E. Todorov, and S. Levine, "Learning dexterous manipulation policies from experience and imitation," *arXiv preprint arXiv:1611.05095*, 2016.
- 15. B. Calli and A. M. Dollar, "Vision-based model predictive control for within-hand precision manipulation with underactuated grippers," in 2017 IEEE International Conference on Robotics and Automation (ICRA). IEEE, 2017, pp. 2839–2845.
- B. Sundaralingam and T. Hermans, "Relaxed-rigidity constraints: kinematic trajectory optimization and collision avoidance for in-grasp manipulation," *Autonomous Robots*, vol. 43, no. 2, pp. 469–483, 2019.

- 17. H. Van Hoof, T. Hermans, G. Neumann, and J. Peters, "Learning robot in-hand manipulation with tactile features," in 2015 IEEE-RAS 15th International Conference on Humanoid Robots (Humanoids). IEEE, 2015, pp. 121–127.
- 18. S. Abondance, C. B. Teeple, and R. J. Wood, "A dexterous soft robotic hand for delicate in-hand manipulation," *IEEE Robotics and Automation Letters*, vol. 5, no. 4, pp. 5502–5509, 2020.
- 19. A. Bhatt, A. Sieler, S. Puhlmann, and O. Brock, "Surprisingly robust in-hand manipulation: An empirical study," *Robotics: Science and Systems (RSS)*, 2021.
- B. Calli, A. Kimmel, K. Hang, K. Bekris, and A. Dollar, "Path planning for within-hand manipulation over learned representations of safe states," in *International Symposium on Experimental Robotics*. Springer, 2018, pp. 437–447.
- 21. H. Zhu, A. Gupta, A. Rajeswaran, S. Levine, and V. Kumar, "Dexterous manipulation with deep reinforcement learning: Efficient, general, and low-cost," in *2019 International Conference on Robotics and Automation (ICRA)*. IEEE, 2019, pp. 3651–3657.
- 22. A. Rajeswaran, V. Kumar, A. Gupta, G. Vezzani, J. Schulman, E. Todorov, and S. Levine, "Learning complex dexterous manipulation with deep reinforcement learning and demonstrations," *Robotics: Science and Systems (RSS)*, 2017.
- 23. G. Khandate, M. Haas-Heger, and M. Ciocarlie, "On the feasibility of learning finger-gaiting in-hand manipulation with intrinsic sensing," in 2022 International Conference on Robotics and Automation (ICRA). IEEE, 2022, pp. 2752–2758.
- 24. A. S. Morgan, K. Hang, B. Wen, K. Bekris, and A. M. Dollar, "Complex in-hand manipulation via compliance-enabled finger gaiting and multi-modal planning," *IEEE Robotics and Automation Letters*, vol. 7, no. 2, pp. 4821–4828, 2022.

- R. Jeong, J. T. Springenberg, J. Kay, D. Zheng, Y. Zhou, A. Galashov, N. Heess, and F. Nori, "Learning dexterous manipulation from suboptimal experts," arXiv preprint arXiv:2010.08587, 2020.
- L. Sievers, J. Pitz, and B. Bäuml, "Learning purely tactile in-hand manipulation with a torque-controlled hand," in 2022 International Conference on Robotics and Automation (ICRA), 2022, pp. 2745–2751.
- 27. A. Allshire, M. Mittal, V. Lodaya, V. Makoviychuk, D. Makoviichuk, F. Widmaier, M. Wüthrich, S. Bauer, A. Handa, and A. Garg, "Transferring dexterous manipulation from gpu simulation to a remote real-world trifinger," arXiv preprint arXiv:2108.09779, 2021.
- 28. D. Chen, B. Zhou, V. Koltun, and P. Krähenbühl, "Learning by cheating," in *Conference on Robot Learning*. PMLR, 2020, pp. 66–75.
- 29. G. B. Margolis, T. Chen, K. Paigwar, X. Fu, D. Kim, S. Kim, and P. Agrawal, "Learning to jump from pixels," 2021.
- 30. A. Kumar, Z. Fu, D. Pathak, and J. Malik, "Rma: Rapid motor adaptation for legged robots," *Robotics: Science and Systems (RSS)*, 2021.
- 31. J. Lee, J. Hwangbo, L. Wellhausen, V. Koltun, and M. Hutter, "Learning quadrupedal locomotion over challenging terrain," *Science robotics*, vol. 5, no. 47, p. eabc5986, 2020.
- 32. G. B. Margolis, G. Yang, K. Paigwar, T. Chen, and P. Agrawal, "Rapid locomotion via reinforcement learning," *Robotics: Science and Systems (RSS)*, 2022.
- 33. J. Tobin, R. Fong, A. Ray, J. Schneider, W. Zaremba, and P. Abbeel, "Domain randomization for transferring deep neural networks from simulation to the real world," in 2017

- *IEEE/RSJ* international conference on intelligent robots and systems (IROS). IEEE, 2017, pp. 23–30.
- 34. N. C. Dafle, A. Rodriguez, R. Paolini, B. Tang, S. S. Srinivasa, M. Erdmann, M. T. Mason, I. Lundberg, H. Staab, and T. Fuhlbrigge, "Extrinsic dexterity: In-hand manipulation with external forces," in *2014 IEEE International Conference on Robotics and Automation (ICRA)*. IEEE, 2014, pp. 1578–1585.
- 35. M. Ahn, H. Zhu, K. Hartikainen, H. Ponte, A. Gupta, S. Levine, and V. Kumar, "Robel: Robotics benchmarks for learning with low-cost robots," in *Conference on Robot Learning*. PMLR, 2020, pp. 1300–1313.
- 36. J. L. Hintze and R. D. Nelson, "Violin plots: a box plot-density trace synergism," *The American Statistician*, vol. 52, no. 2, pp. 181–184, 1998.
- 37. J. Xu, T. Chen, L. Zlokapa, M. Foshey, W. Matusik, S. Sueda, and P. Agrawal, "An end-to-end differentiable framework for contact-aware robot design," *Robotics: Science and Systems*, 2021.
- 38. S. Brahmbhatt, C. Ham, C. C. Kemp, and J. Hays, "ContactDB: Analyzing and predicting grasp contact via thermal imaging," in *The IEEE Conference on Computer Vision and Pattern Recognition (CVPR)*, 6 2019.
- 39. V. Makoviychuk, L. Wawrzyniak, Y. Guo, M. Lu, K. Storey, M. Macklin, D. Hoeller, N. Rudin, A. Allshire, A. Handa, and G. State, "Isaac gym: High performance GPU based physics simulation for robot learning," in *Thirty-fifth Conference on Neural Information Processing Systems Datasets and Benchmarks Track*, 2021.
- 40. S. Ross, G. Gordon, and D. Bagnell, "A reduction of imitation learning and structured prediction to no-regret online learning," in *Proceedings of the fourteenth international con-*

- *ference on artificial intelligence and statistics*. JMLR Workshop and Conference Proceedings, 2011, pp. 627–635.
- 41. J. Schulman, F. Wolski, P. Dhariwal, A. Radford, and O. Klimov, "Proximal policy optimization algorithms," *arXiv preprint arXiv:1707.06347*, 2017.
- 42. A. Y. Ng, D. Harada, and S. Russell, "Policy invariance under reward transformations: Theory and application to reward shaping," in *Icml*, vol. 99, 1999, pp. 278–287.
- 43. C. Choy, J. Gwak, and S. Savarese, "4d spatio-temporal convnets: Minkowski convolutional neural networks," in *Proceedings of the IEEE Conference on Computer Vision and Pattern Recognition*, 2019, pp. 3075–3084.
- 44. K. Cho, B. Van Merriënboer, C. Gulcehre, D. Bahdanau, F. Bougares, H. Schwenk, and Y. Bengio, "Learning phrase representations using rnn encoder-decoder for statistical machine translation," *arXiv preprint arXiv:1406.1078*, 2014.
- 45. J. Tan, T. Zhang, E. Coumans, A. Iscen, Y. Bai, D. Hafner, S. Bohez, and V. Vanhoucke, "Sim-to-real: Learning agile locomotion for quadruped robots," *arXiv* preprint *arXiv*:1804.10332, 2018.
- 46. N. Hansen, S. D. Müller, and P. Koumoutsakos, "Reducing the time complexity of the derandomized evolution strategy with covariance matrix adaptation (cma-es)," *Evolutionary computation*, vol. 11, no. 1, pp. 1–18, 2003.
- 47. L. Downs, A. Francis, N. Koenig, B. Kinman, R. Hickman, K. Reymann, T. B. McHugh, and V. Vanhoucke, "Google scanned objects: A high-quality dataset of 3d scanned household items," *arXiv preprint arXiv:2204.11918*, 2022.

- 48. A. X. Chang, T. Funkhouser, L. Guibas, P. Hanrahan, Q. Huang, Z. Li, S. Savarese, M. Savva, S. Song, H. Su, J. Xiao, L. Yi, and F. Yu, "ShapeNet: An Information-Rich 3D Model Repository," Stanford University Princeton University Toyota Technological Institute at Chicago, Tech. Rep. arXiv:1512.03012 [cs.GR], 2015.
- 49. K. Mamou, E. Lengyel, and A. Peters, "Volumetric hierarchical approximate convex decomposition," in *Game Engine Gems 3*. AK Peters, 2016, pp. 141–158.
- 50. D.-A. Clevert, T. Unterthiner, and S. Hochreiter, "Fast and accurate deep network learning by exponential linear units (elus)," 4th International Conference on Learning Representations, ICLR, 2015.
- 51. D. P. Kingma and J. Ba, "Adam: A method for stochastic optimization," in *3rd International Conference on Learning Representations (ICLR)*, 2015.
- 52. K. Daniilidis, "Hand-eye calibration using dual quaternions," *The International Journal of Robotics Research*, vol. 18, no. 3, pp. 286–298, 1999.
- 53. M. Quigley, K. Conley, B. Gerkey, J. Faust, T. Foote, J. Leibs, R. Wheeler, A. Y. Ng *et al.*, "ROS: an open-source robot operating system," in *ICRA workshop on open source software*, vol. 3, no. 3.2. Kobe, Japan, 2009, p. 5.
- P. Florence, C. Lynch, A. Zeng, O. A. Ramirez, A. Wahid, L. Downs, A. Wong, J. Lee,
 I. Mordatch, and J. Tompson, "Implicit behavioral cloning," in *Conference on Robot Learning*. PMLR, 2022, pp. 158–168.
- 55. Y. Zhou, C. Barnes, J. Lu, J. Yang, and H. Li, "On the continuity of rotation representations in neural networks," in *Proceedings of the IEEE/CVF Conference on Computer Vision and Pattern Recognition*, 2019, pp. 5745–5753.

Supplementary Materials

The PDF file includes:

Sections S1 to S5

Figs. S1 to S8

Tables S1 to S4

Other Supplementary Materials for this manuscript include the following:

Movies S1 to S2

S1 Nomenclature

Table S1: nomenclature

Symbol	Meaning	Symbol	Meaning	
\mathbb{B}	the Big dataset	$ar{ heta}$	threshold value for orientation distance	
$\mathbb S$	the Small dataset	$ar{\dot{q}}$	threshold value for joint velocity norm	
o	observation	\bar{a}	threshold value for action norm	
\boldsymbol{a}	action command	\bar{v}	threshold value for linear velocity norm	
$ar{m{a}}$	smoothed action command	$ar{\omega}$	threshold value for angular velocity norm	
π	policy	\bar{p}	threshold value for object's distance from the har	
r	reward	$\epsilon_{ heta}$	a constant in reward function	
${\cal E}$	expert	$oldsymbol{P}$	point cloud	
${\cal S}$	student	l_j	j^{th} link on the hand	
γ	discount factor	G	number of fingers	
α	smoothing factor for action	\boldsymbol{p}^{f_i}	fingertip position of i^{th} finger	
$oldsymbol{q}$	joint positions	$oldsymbol{ au}_t$	joint torques	
$\Delta\theta$	the distance between the object's current orientation and goal orientation	$oldsymbol{p}^o$	object center position	
$\dot{m{q}}$	joint velocities	R	rotation matrix	
$oldsymbol{v}^o$	object's linear velocity	$oldsymbol{p}$	position	
$oldsymbol{\omega}^o$	object's angular velocity	M	number of links on a hand	
z	embedding vector	C	robot	
$oldsymbol{A}(\cdot)$	a sequence of action commands	Λ	the entire space of possible dynamics parameters	
λ	dynamics parameters of a robot	h	score function for trajectory similarity	
f	frequency	$\mathcal{N}()$	Gaussian distribution	
F_d^o	disturbance force on the object	$\mathcal{U}()$	uniform distribution	
m^o	object's mass			

S2 Experiment details

S2.1 Object datasets

We use the following object sets:

• **Big dataset** (\mathbb{B}): is used for training policies. It is a collection of 150 objects from internet sources, including Google Scanned Objects (47) and ShapeNet (48). The chosen objects cover a wide range of complex and non-convex shapes, such as cars, shoes, animals, etc. (see

Figure S1). We only choose objects that are asymmetric, or only reflective symmetric, which mitigates the multi-modality issue in defining object poses (7). However, such a choice for training does not restrict our system from reorienting symmetric objects, a claim we empirically evaluate.

• Small dataset (\mathbb{S}): is used for evaluating generalization performance. It contains 12 objects from the ContactDB (38) dataset with no overlapping object shape with dataset \mathbb{B} . We use a subset of 5 objects from \mathbb{S} to evaluate out-of-distribution (OOD) performance in the real world.

Object dataset preprocessing In order to make the objects manipulable by the robot hands, we need to scale their meshes to proper sizes. In simulation, we center each mesh and manually scale each object mesh to a proper size compared to the robot hand size. Overall, the longest side of the objects' bounding boxes lies in the range of [0.095, 0.165]m. The mass of each object is randomly sampled from [0.03, 0.18]kg. The mass of the objects used in the real-world tests is shown in Table S3.

Convex Decomposition We use V-HACD (49) to perform an approximate convex decomposition on the object and the robot hand meshes for fast collision detection in the simulator. The decomposition resolution is 100,000.

S2.2 Training setup

Observation space for the teacher policy The inputs to the teacher policy, $o_t^{\mathcal{E}} \in \mathbb{R}^{19G+21}$, include joint positions (\mathbb{R}^{3G}) and velocities (\mathbb{R}^{3G}), fingertip pose (\mathbb{R}^{7G}) and velocities (\mathbb{R}^{6G}), object pose (\mathbb{R}^{7}) and velocity (\mathbb{R}^{6}), target orientation expressed as a quaternion (\mathbb{R}^{4}), and the rotation difference between current and target object orientation expressed as a quaternion (\mathbb{R}^{4}), where G represents the number of fingers. The pose of each finger is represented by a position (\mathbb{R}^{3}) and an orientation component (quaternion; \mathbb{R}^{4}).

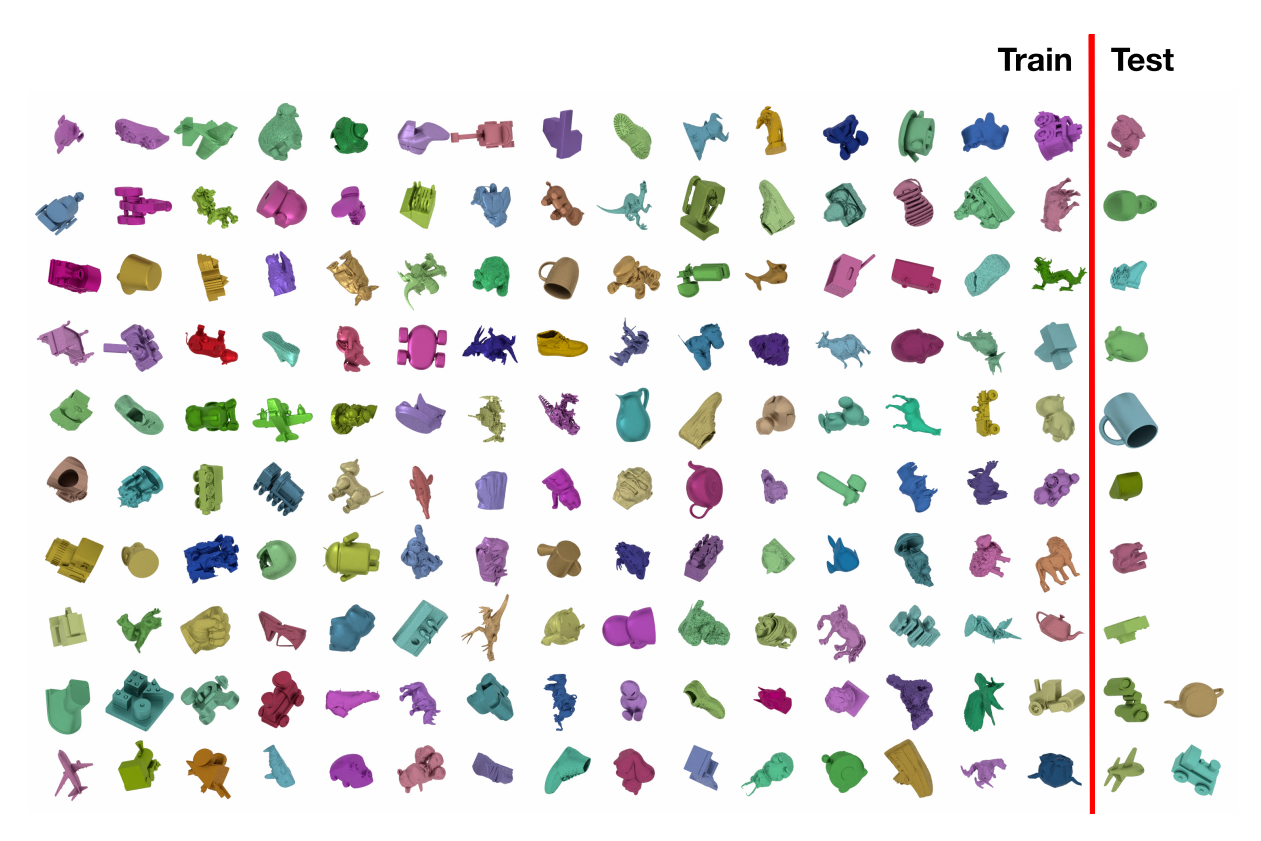


Fig. S1 Object dataset. On the left of the red line, we show the dataset \mathbb{B} (the training dataset). And on the right of the red line, we show the dataset \mathbb{S} (the testing dataset in simulation).

Teacher policy architecture Our teacher policy is an MLP network consisting of three hidden layers (512, 256, 256 neurons) and ELU activation functions (50). We use Adam (51) to optimize the networks.

GPU hardware In our experiments, we use one NVIDIA GeForce RTX 3090 for training the teacher policies, and one NVIDIA Tesla V100 for training the student (vision) policies.

Hyper-parameters Table S2 lists the hyper-parameters used in the experiments.

Point cloud voxelization The point cloud input to the policy network has no color information and is voxelized in a resolution of 0.005m.

Table S2: Hyper-parameter Setup

Hyperparameter	Value	Hyperparameter	Value	Hyperparameter	Value
		Teacher policy			
# of envs	32000	batch size	64000	# of rollout steps per policy update	8
GAE lambda	0.95	Reward discount 0.9		# of policy update epochs after each rollout	12
Actor learning rate	0.0003	Critic learning rate	0.001	PPO clip range	0.1
$\epsilon_{ heta}$	0.4 rad	c_1	1	c_2	800
c_3	-1	c_4	-20	c_5	-100
c_6	-1	c_7	-2	$ar{p}$	0.15
$ar{p}_z$	0.16	$ar{\dot{q}}$	0.25	$ar{v}$	0.04
$ar{\omega}$	0.5	c_d	15		
		Student policy			
# of envs (Stage 1/Stage 2) 400/		batch size (Stage 1/Stage 2)	40/20	# of pts sampled from each CAD model	500
# of pts sampled from realistically rendered point cloud	6000	learning rate	0.0003	# of rollout steps per policy update	80

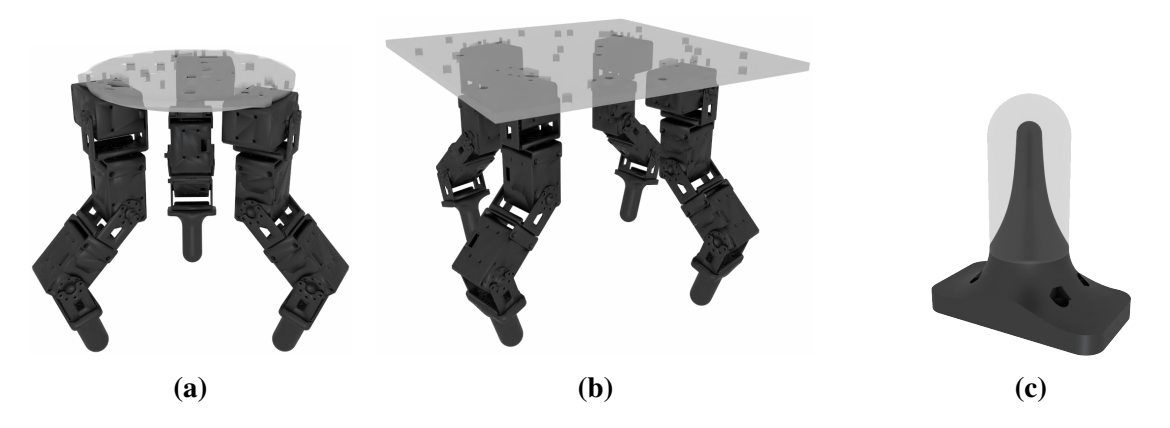


Fig. S2 (a): three-fingered robot hand. (b): four-fingered robot hand. (c): fingertips with a rounded skeleton and the grey shell represents soft elastomer.

S2.3 Real-world setup

We used two robot hands in our experiments: a three-fingered hand (D'Claw) and a four-fingered hand. The three and four-fingered hands consist of nine and twelve Dynamixel motors, respectively. The hands are fixed on an 80/20 aluminum frame. Since our goal is to construct a real-world ready reorientation system that can be used on a mobile manipulator in the future,

we only use *one* RealSense D415 camera to observe the robotic hand manipulate the object. The robot and camera are calibrated using the dual quaternions method (52). We only perform camera calibration on one of the robot fingers, and the ArUco marker is attached to the fingertip. Due to the limits on the finger's motion (3 DoFs), it is impossible to span a broad range of positions for the ArUco marker, resulting in noisy calibration with noticeable errors. Empirically we found such errors didn't impact the performance of our system. We use ROS (53) for communication with the Dynamixel motors and use a threading lock to prevent simultaneous reading and writing on the motors as Dynamixel motors use a half-duplex UART (Universal Asynchronous Receiver Transmitter) for communication. Each Dynamixel motor is controlled via position control in 12Hz. The Dynamixel-specific parameters noted in Dynamixel's control table are set as follows: *P* is 200, and the *D* gain is 10. The observations available to the controller are the joint positions of each motor and the depth image from the Realsense camera.

Real-world observation The observation consists of the joint positions of each motor in the robotic hand and the depth image from the RealSense camera. We convert both these sensory inputs into a point cloud. The joint angles are converted into a point cloud as follows: Using the robot's CAD model, we uniformly sample points on each link and cache it. Given a sequence of joint positions, we use forward kinematics to compute the pose of each link and accordingly transform each of the associated pre-cached point clouds. We call the concatenated point cloud of all links as *proprioceptive point cloud*. The depth image is also converted into a 3D point cloud (*exteroceptive point cloud*). Both point clouds are merged and used as inputs to our policy. We do not assume access to any other sensory information.

Stopping criteria The robot stops when it is deemed successful as per the success criteria described above. Evaluating the success criteria requires knowledge of object motion (*object motion criterion*), orientation distance (*orientation criterion*), and fingertip motion (*finger mo-*

tion criterion). While we can measure the fingertip motion $(\dot{q}_t \text{ and } a_t)$ in the real world, we cannot directly measure the object's motion and pose. To obtain the orientation error, we train a predictor that re-uses features from the policy network to predict $|\Delta\theta_t|$ (see Figure 7a). Predicting object motion from point clouds is harder, and we found it unnecessary to estimate. We found that satisfying only the *orientation criterion* and *finger motion criterion* is sufficient to successfully stop the object at the target orientation. We also found it sufficient only to check $||a_t|| < \bar{a}$ to detect finger motion during real-world deployment.

Real-world quantitative evaluation setup We set up a motion capture system using six OptiTrack cameras to quantitatively evaluate the policy performance in the real world. We add markers on the surface of evaluation objects. Even though the added markers add little bumps on the object's surface and therefore change the dynamics, we found our policies to be robust enough to deal with these changes. The output of the motion capture system is the object pose. We use the tracked object pose when the stopping criteria are satisfied to compute the error from the target orientation. We only use the motion capture system for quantitative evaluation, and it is not required by our system to reorient objects. Note that the motion capture system can fail to track the objects occasionally when the fingers heavily occluded the markers. When it happens, we discard this test as we cannot get a quantitative error in this case.

S2.4 Computing the orientation error for symmetric objects

With symmetric objects, it is hard to determine whether the controller completes the task or not unless we know in what way the object is symmetric. We can still use a motion capture system to get the object's pose. However, we cannot directly compute the distance between the orientation from the motion capture system, and the goal orientation as there exist many different orientations that make objects look similar. Therefore, we need to find out all such

possible goal orientations. While scaling this up to a wide variety of objects is challenging, in our experiments, we tested on two symmetric objects (a rectangular cuboid and a cube) whose symmetric axes can be easily enumerated. In other words, on the rectangular cuboid and cube, we can easily identify all possible rotational axes upon which the objects can be rotated by some angle and end up with the same visual appearance. Then we compute the distances between the actual object orientation and all possible goal orientations and find the minimum distance.

S3 Fabrication

Fingertip Fabrication We experimented with both rigid and soft fingertips. The rigid fingertips were fabricated using 3D printing. For the soft fingertips, we designed a rigid inner skeleton coated in a soft outer elastomer. The elastomer allows the robot's fingertips to have increased compliance and friction when interacting with the plastic objects, while the plastic internal skeleton helps maintain the shape of the fingertips without too much deformation, similar to a human finger. The design for the internal skeleton used is shown in Figure S2.

The fingertip skeletons and molds for the elastomer are 3D printed on the Markforge Onyx One using the Onyx filament. To help improve the adhesion of the silicone to the Onyx material, the skeletons are sanded with 400-grit sandpaper, corona treated, and primed using the Dow DOWSIL P5200 Adhesion Promoter.

The gel coating for both the fingertip designs are made from Smooth-On's Ecoflex platinum-catalyzed silicone. The elastomer has a shore hardness of 00-10 and exhibits a tacky finish when fully cured. A ratio of 1:0.008:0.005 by weight of the Ecoflex mixture (Parts A and B combined), Smooth-On Silc Pig White, and Smooth-On Silc Pig Black are combined to provide the gray color of the fingertips. To ensure the surface of the gel elastomer is smooth, XTC-3D is applied to the inside of the 3D printed molds to smooth out any texture. The uncured Ecoflex mixture is poured into the molds and degassed to eliminate air bubbles from forming on the

elastomer's surface. The skeletons are pushed into the top-down molds and left to cure at room temperature for 4 hours.

Object Fabrication We use 3D printing to fabricate objects that are used for quantitative evaluation. Each object was printed with a 0.25mm layer height on the Lulzbot TAZ Pro Dual Extruder using PolyTerra PLA filament in different colors. Table \$3 lists the mass of each object used in the real-world experiments. Note that to test the transfer of our results, we also included real household objects in our test set.

Object Mass (g) Object Mass (g) Object Mass (g) Object Mass (g) 158.0 95.0 111.1 116.9 70.3 151.8 104.3 92.1 106.3 140.9 86.8 117.6 50.1 148.1 162.1 106.1 180.9 60.5 104.1 85.7 127.9 137.1 67.1 244.0

Table S3: Object mass.

S4 Overcoming sim-to-real gap

S4.1 Dynamics Identification

Action commands In this work, we send two types of action commands to the robot and collect the joint movement trajectories. The first type of action command is a step command $(\mathbf{A}(t) = c \text{ where } c \text{ is a constant joint position command})$, i.e., we collect the step responses

from the motors. The second type of action command is sin-wave action commands in different frequencies. The sin-wave command is $A(t) = \sin(2\pi f t)$ where $f \in [0.05, 1.5]$ Hz. For both types of action commands, we scale the amplitude proportionally to the joint limit of each joint.

Dynamics parameters to be identified We perform dynamics identification on the joint stiffness, damping, and velocity limit. Only one finger on the real robot hand is used to collect the response trajectories. Each joint on the finger is identified individually, and the same group of dynamics parameters of the finger is applied to the remaining fingers in the simulator.

Response curves In Figure S3, we show the response curves of the three joints on a finger given a sequence of action commands both in simulation and in the real world. We can see that after the dynamics identification, the simulated joints can give a similar response as the real joints. We also observe that the real joints (the orange lines) usually have a slightly slower response than the simulated joints (the green lines). This is due to the latency of a real robot hand system. We did not model the latency in simulation and found that our controller still works on the real robot hands. It is possible that including the latency in simulation might further improve the controller's real-world performance, for which we leave the investigation to future work.

S4.2 Robust policy learning

S4.2.1 Observation and action noise

We add Gaussian noise to the action commands (Table S4) for training all policies. The teacher policy is trained with state noise as detailed in Table S4. The vision policies are trained with data augmentation on the point cloud observation. With a probability of p = 0.4, we add Gaussian noise $\mathcal{N}(0, 0.004)$ to the point positions. Independently, with a probability of p = 0.4, we randomly drop out $q \in [0, 20]$ percent of the points.

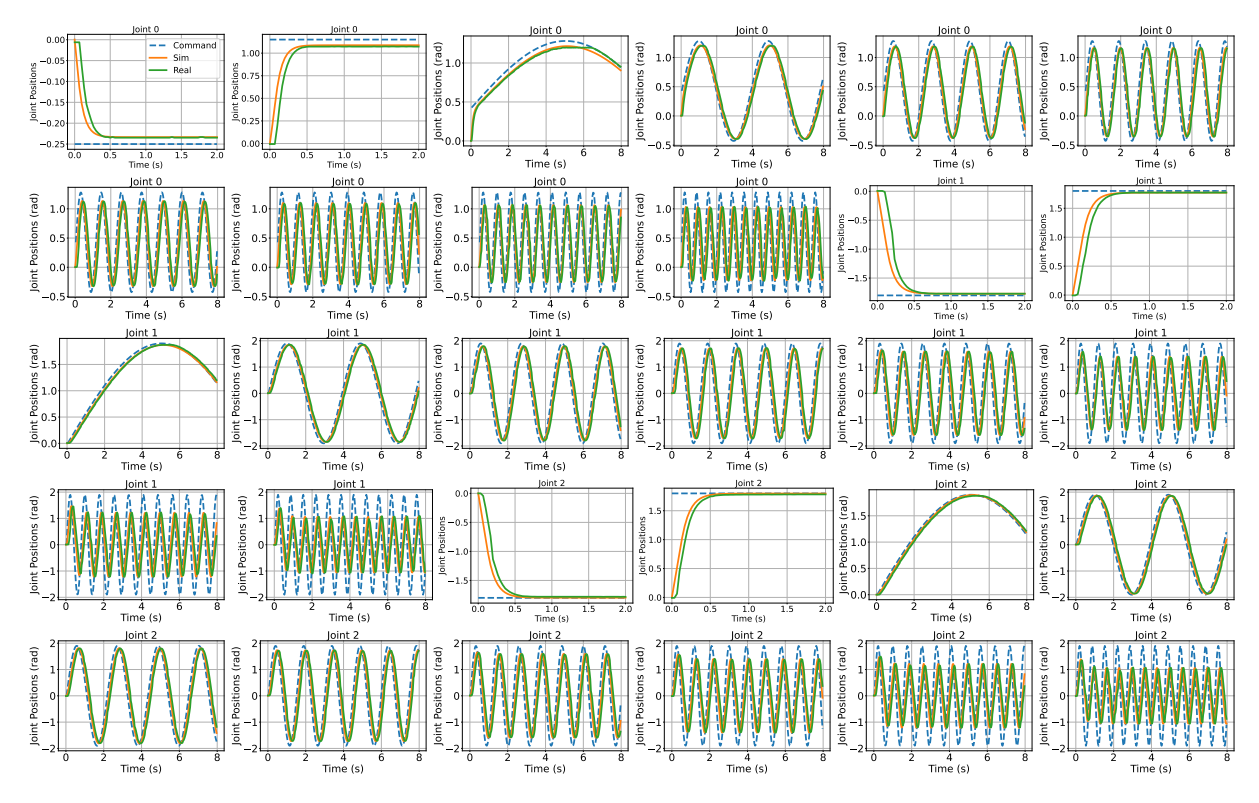


Fig. S3 We show the results of dynamics identification on one finger. We plot three curves: (1) the command sent to the joint, (2) the joint response in simulation with the identified dynamics parameters, (3) the joint response in the real world. We can see that the identified dynamics parameters allow the joints in simulation to move similarly to real joints. The joint IDs [0, 1, 2] correspond to the top joint, the middle joint, and the bottom joint in Figure S2a respectively.

S4.2.2 Dynamics randomization

We train policies with small randomization in the joint dynamic parameters: the link mass, joint friction, and joint damping. We add large randomization to the object dynamics parameters such as mass friction, and restitution. Table S4 lists the amount of randomization we add to the dynamics parameters and the observation/action noise.

S4.2.3 Disturbance force on the object

With a probability p = 0.2 at each time step, we apply a disturbance force with a magnitude of $F_d^o = c_d m^o$ where m^o is the object mass, c_d is a coefficient and a random force direction

Table S4: Dynamics Randomization and Noise

Parameter	Range	Parameter	Range	Parameter	Range
state observation	$+\mathcal{N}(-0.002, 0.002)$	action	$+\mathcal{N}(0, 0.05)$	joint stiffness	$\times \mathcal{U}(0.8, 1.2)$
joint damping	$\times \mathcal{U}(0.8, 1.2)$	link mass	$\times \mathcal{U}(0.8, 1.2)$	friction for robot, objects	U(0.24, 1.6)
friction for table	$\mathcal{U}(0.05, 1.0)$	restitution	U(0.0, 1.0)	object size scale	$\mathcal{U}(0.95, 1.05)$
object mass	$\mathcal{U}(0.009, 0.324)$ kg				

 $[\]mathcal{N}(\mu, \sigma)$: Gaussian distribution with mean μ and standard deviation σ .

sampled in the SO(3) space.

S5 Additional results

S5.1 Symmetric object reorientation

Learning visual policies to reorient symmetric objects is challenging because objects in different but symmetrical pose appear similar leading to multimodality (7): Given a target orientation, many different poses of symmetric object match the goal configuration visually, leading to different but equally good action sequences. It is challenging to learn a stochastic vision policy that explicitly accounts for multi-modality. An alternative is to use implicit models (54). However, these models are compute inefficient, which prevents their use in a real-time controller.

The key intuition behind how we overcome this problem is that we need to account for multi-modality only at training time to ensure that a correct action sequence is not incorrectly penalized. However, at deployment, it is not necessary to distinguish between modes, and reorienting the object into any of the equivalent symmetric configurations would suffice. We bypass the problem of accounting for multi-modality at training time by using only unimodal objects – i.e., asymmetric or reflective-symmetric objects. Our hypothesis was that if we are able to successfully learn a controller that operates over a diverse range of asymmetric shapes, it may also generalize to symmetric objects.

 $[\]mathcal{U}(a,b)$: uniform distribution between a and b.

^{+:} the sampled value is added to the original value of the variable. ×: the original value is scaled by the sampled value.

To verify if this hypothesis was true, we tested our controller on two symmetric objects (a rectangular cuboid and a cube) with table support. Figure 4f shows that our controller still works reasonably well. Nonetheless, in this case, the orientation error tends to be higher than non-symmetric objects (Figure 4e). While it is hard to pinpoint whether this is due to the performance drop in predicting the actions or predicting when the goal orientation is reached, we believe the latter plays a bigger role.

S5.2 Using a different encoder for goal

As shown in Figure S4b, we also found that stacking the goal object point cloud onto the scene point cloud and feeding it as a whole into the 3D CNN encoder (Figure 7b) leads to faster policy learning than using two separate 3D CNN encoders (Figure S4a) to process the scene point cloud and the goal object point cloud.

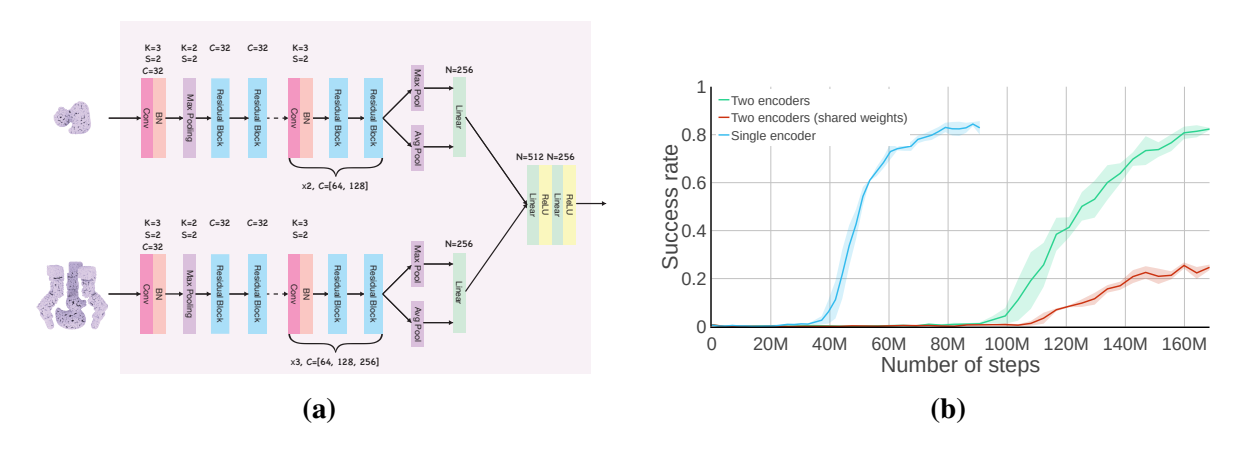


Fig. S4 (a): we tried using separate encoders for the goal point cloud and the scene point cloud. **(b)** shows that using separate encoders leads to considerably slower policy learning than using a single encoder on merged goal and scene point clouds.

S5.3 Stage 0: speeding up vision policy training with visual pre-training

Can we further speed up the vision policy learning? As shown in Figure 7a, our policy network is a recurrent network. Training a sequence model can take longer training time. We investigated

whether we can first pre-train the vision network component (sparse 3D CNN) in the policy network without involving the RNN component (Stage 0), and then fine-tune the policy with the pre-trained vision network (Stage 1). To pre-train the vision network, we explored various representation learning techniques, such as learning a forward/inverse dynamics model and reconstructing the input point cloud to pre-train the vision network. To our surprise, while most pre-training techniques lead to mild, if any, improvement in the policy learning speed, it's beneficial to first train the vision network to predict some low-dimensional state information of the system. More specifically, in the pre-training stage, the vision network is trained to predict the object category, the distance between the object's orientation and the goal orientation, and the joint positions of the robot hand (q_t) . Note that we do not predict object pose, which would require a definition of reference frame on the objects. To further speed up the training, we do not use simulation at all to generate the training data at this stage. Instead, we generate completely random synthetic data for training (Figure S5a). First, we convert meshes of the robot links and objects into their corresponding canonical point clouds. Next, we randomly sample joint angles and use forward kinematics to get the pose of each robot link and randomly sample object poses and goal poses. Finally, we transform the canonical point clouds of each part according to their poses and get the point cloud of the entire scene.

For rotational distance prediction, we experimented with two representations. The first one is the 6D representation (55) of the relative rotation matrix $\mathbf{R}_t^o(\mathbf{R}^g)^{-1}$ between the object's current orientation \mathbf{R}_t^o and goal orientation \mathbf{R}^g . The second one is the scalar distance between the two rotation matrices ($\Delta\theta_t$). We found that pre-training the vision network to predict the scalar distance leads to faster convergence during pre-training than predicting the 6D representation of the relative rotation matrix. In addition, we experimented with two ways of using the output of the vision network for the state prediction tasks: (1) three prediction tasks use the same embedding (Figure S5b), (2) we split the vision network output into three parts (object embedding

 z^o , goal embedding z^g , robot embedding z^r), and each prediction task only uses the relevant embedding (Figure S5c). When training to predict the scalar rotational distance, we don't find these two ways of using the vision network output to make a difference. However, when training to predict the 6D representation of the rotational distance, splitting the embedding leads to a significantly faster pre-training (Figure S5d). After the pre-training converges, we proceed to Stage 1 using the pre-trained vision network backbones. We found that all four pre-training schemes lead to a substantial and similar speedup for policy learning (Figure S5e). We also did an ablation study on the importance of different pre-training tasks in Section S5.4.

S5.4 Ablation on the prediction tasks for vision network pre-training

We perform ablation study on different prediction tasks for pre-training the vision networks in Stage 0. In Figure S6, *Full* representing the case of training to predict all three tasks (the scalar rotational distance, the joint positions, and the object category) with the single embedding architecture. And our ablation studies remove each prediction task individually. As shown in Figure S6, removing the rotational distance prediction task makes the pretraining much easier (loss goes down much faster), but it also negatively impacts the benefit of pre-training the most. It implies that the task of predicting the rotational distance is most useful for pre-training the vision network. Removing the task of predicting the joint positions slightly reduces the benefit of pre-training. Removing the task of predicting the object category has almost no impact on the policy learning.

S5.5 Analysis for object reorientation in the air in simulation

We can get three outcomes when using the four-fingered hand reorienting objects in the air: the episode succeeds (*Success*), the controller stops the object with an orientation error bigger than 0.4rad (*Orientation error*), the object falls (*Object falls*), or the controller runs out of time and

fails to reach the goal orientation (*Time out*). To see the ratio of each case, we tested the vision controller, which takes as input the realistically rendered point cloud, on the twelve objects in Figure 3a in simulation. We set the testing episode length to 180 time steps, which is equivalent to 15 seconds. For the first 24 time steps (2 seconds), we keep the table below the hand so that the hand can first grasp the objects. After the 24th step, we remove the table and check if the controller can reorient the objects in the air. Note that this is a rough approximation of the real-world testing scenario where we hand over the object to the robot hand and release the object after the hand grasps the object, because when we remove the table, there is no guarantee that the hand happens to grasp the object stably at the 24th time step. Nonetheless, empirically, we found only 10.3% of the 1200 testing episodes have the issue of object falling immediately (we check if the object falls from 24 steps to 30 steps) after the table is removed, suggesting that this is still a reasonable approximation of the real-world testing scenarios. To emulate how we stop the policy in the real world, we also stop the policy in simulation if $|\Delta\theta_t^{pred}| < \bar{\theta}$ (we check the predicted orientation distance from the policy network) and $||a_t|| < \bar{a}$.

Each object is tested 100 times with a random initial pose and goal orientation. We plot the percentage of each case (*Success*, *Orientation error*, *Time out*, *Object falls*) in Figure S7c. In Figure S8c, we show the distribution of the orientation error in non-dropping episodes for all twelve objects. In Figure S8a, we show the comparison between the performance in simulation and in the real world. Similarly, Figure S8d shows the distribution of the episode time of the non-dropping episodes. Figure S8b shows the comparison of the episode time between the simulation and the real world.

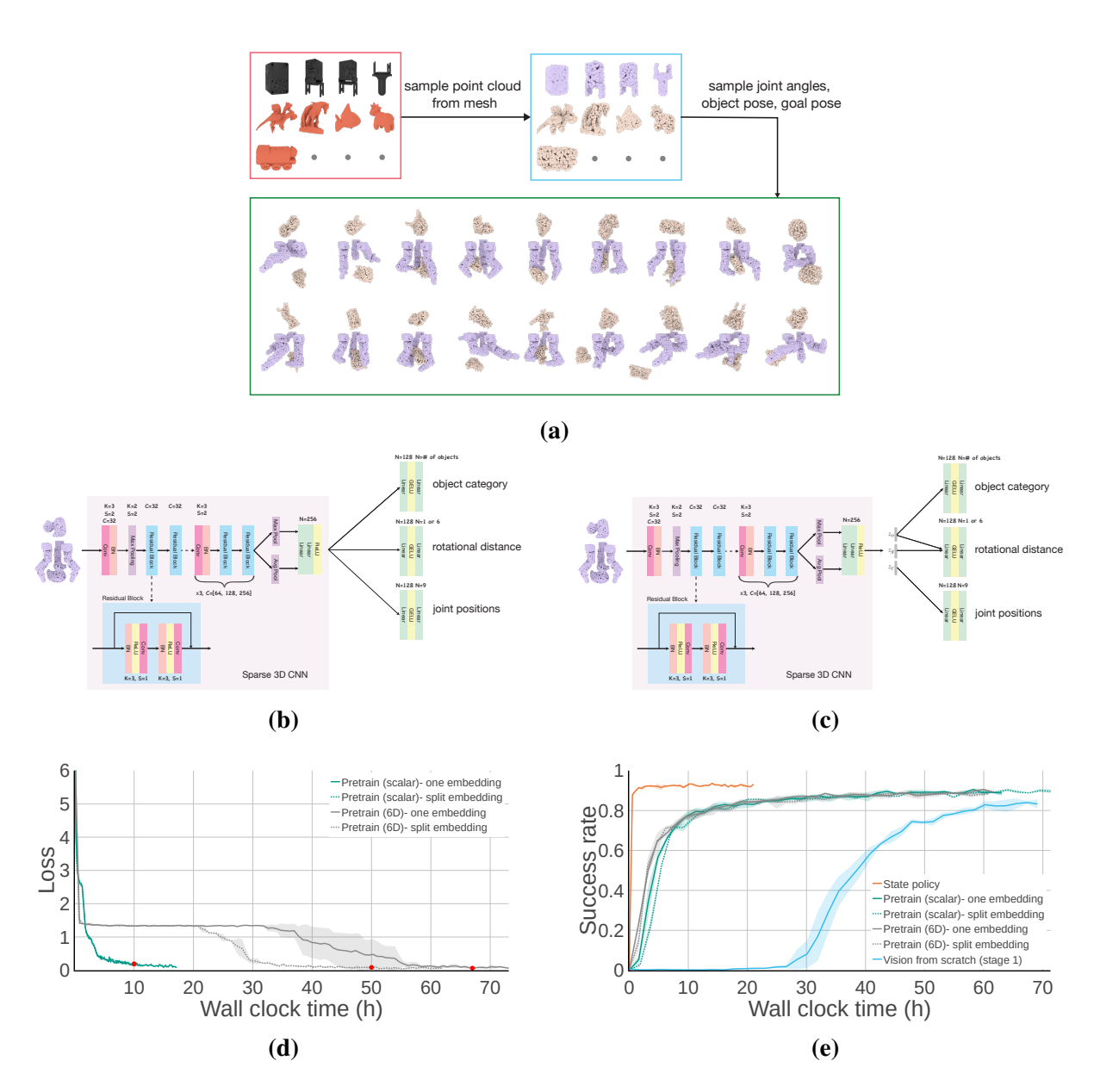


Fig. S5 (a) shows the synthetic data generation in Stage 0. In (b) and (c), we designed two architectures, with the difference being whether the output of the vision network is split into entity-specific embeddings or not. (d) shows the learning curves under different training conditions. The red dots represent the checkpoints we took for policy learning. (e): After the pre-training, we use the vision network as the policy backbone and train the policy with BC. The **State policy** is a student policy that takes as input the joint positions, rotation matrix of the relative orientation, and object position, which can be seen as an upper bound for the vision policy. **Vision from scratch (stage 1)** means the vision policy learning in stage 1 only without stage 0.

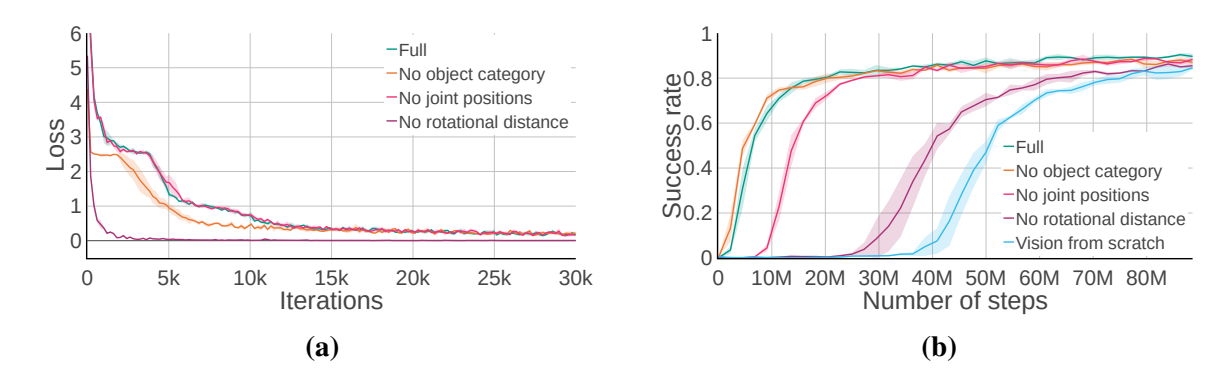


Fig. S6 (a): loss curves for the pre-training in Stage 0. **(b)**: learning curves for training the vision policies with the pre-trained vision networks in Stage 1.

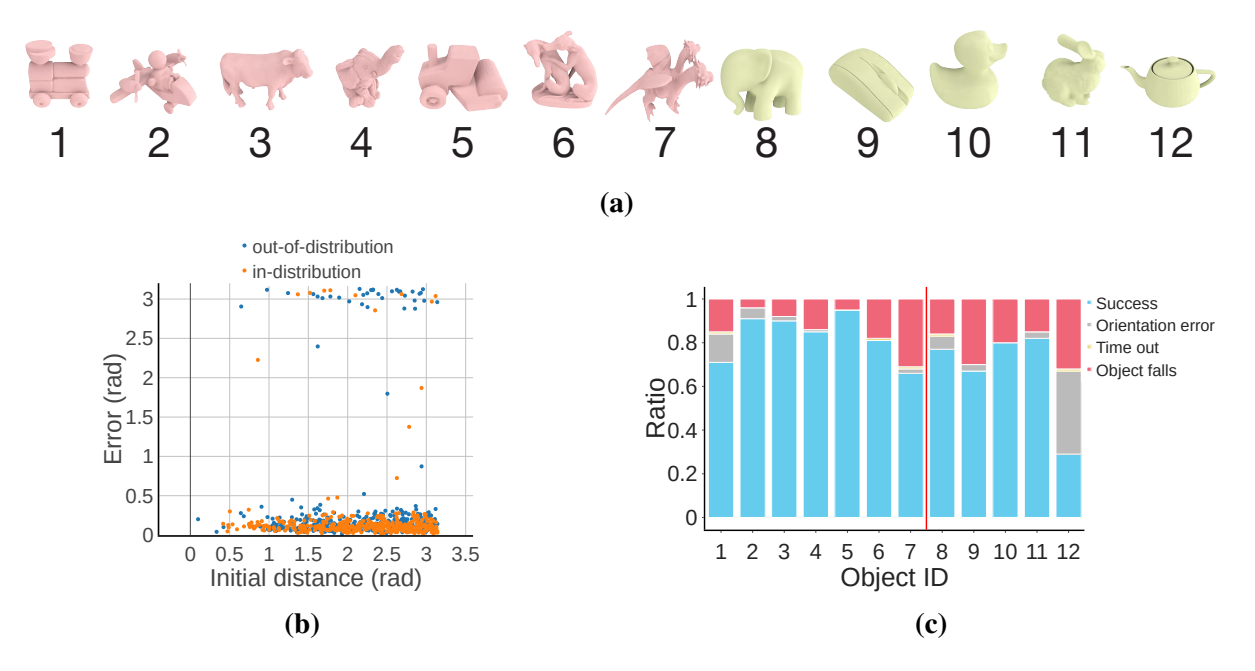


Fig. S7 Tests for object reorientation in the air *in simulation*. We tested each object in Figure 3a 100 times with random initial pose and goal orientation. (a): the objects we used for testing (same as Figure 3a). (b): We show the relationship between the reorientation error and the distance $(\Delta\theta_0)$ between the object's initial and target orientation on non-dropping tests (around 90%). We randomly sub-sample the tests on in-distribution objects to make sure the total numbers of points are the same for in-distribution objects and out-of-distribution objects in this plot. (c): We categorize the testing results for each object into four cases: *Success, Orientation error* (where the controller stops the object with an orientation error greater than 0.4rad), *Time out*, *Object falls*.

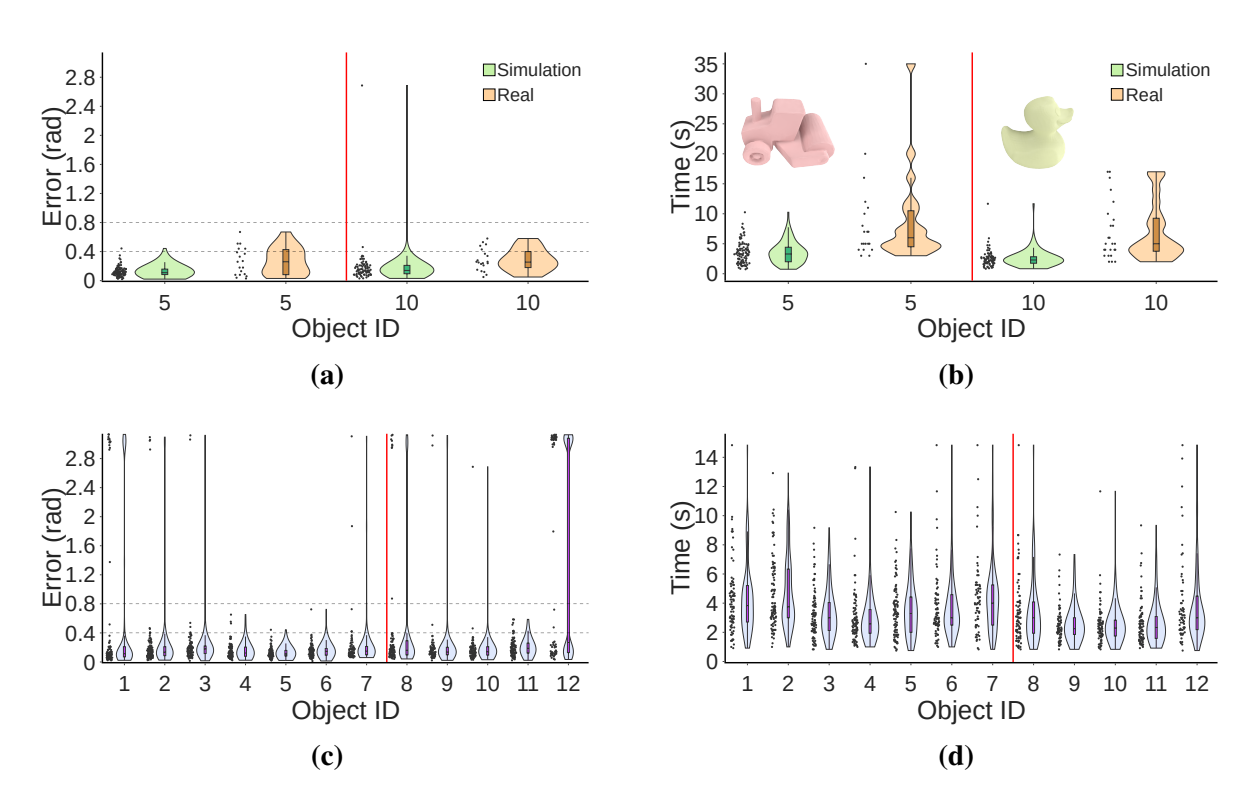


Fig. S8 Following Figure S7, (a) and (b): With object #5 and #10, we compare the distribution of the orientation error and the elapsed time of the episodes in simulation and in the real world. The controller achieves lower error and uses shorter time in simulation. We can see there is still a gap between the simulation and real-world performance. (c) and (d): we show the distribution of the reorientation error and episode time of the non-dropping testing episodes on all twelve objects in simulation.